2007

Detecting molecular properties by various laser-based techniques

Tse-Ming Hsin
Iowa State University

Detecting molecular properties by various laser-based techniques

by

Tse-Ming Hsin

A dissertation submitted to the graduate faculty

in partially fulfillment of the requirements for the degree of

DOCTOR OF PHILOSOPHY

Major: Physical Chemistry

Program of Study Committee:
Edward S. Yeung, Major Professor
Victor S.-Y. Lin
Klaus Schmidt-Rohr
Xueyu Song
Hans U. Stauffer

Iowa State University

Ames, Iowa

2007

To Grandpa, Dad, and Mom,
To Cherry and "little Bobby".

TABLE OF CONTENTS

ABSTRACT

Four different laser-based techniques were applied to study physical and chemical characteristics of biomolecules and dye molecules. These techniques are hole burning spectroscopy, single molecule spectroscopy, time-resolved coherent anti-Stokes Raman spectroscopy and laser-induced fluorescence microscopy.

Results from hole burning and single molecule spectroscopy suggested that two antenna states (C708 & C714) of photosystem I from cyanobacterium *Synechocystis* PCC 6803 are connected by effective energy transfer and the corresponding energy transfer time is ~6 ps. In addition, results from hole burning spectroscopy indicated that the chlorophyll dimer of the C714 state has a large distribution of the dimer geometry.

Direct observation of vibrational peaks and evolution of coumarin 153 in the electronic excited state was demonstrated by using the fs/ps CARS, a variation of time-resolved coherent anti-Stokes Raman spectroscopy. In three different solvents, methanol, acetonitrile, and butanol, a vibration peak related to the stretch of the carbonyl group exhibits different relaxation dynamics.

Laser-induced fluorescence microscopy, along with the biomimetic containers—liposomes, allows the measurement of the enzymatic activity of individual alkaline phosphatase from bovine intestinal mucosa without potential interferences from glass surfaces. The result showed a wide distribution of the enzyme reactivity. Protein structural variation is one of the major reasons that are responsible for this highly heterogeneous behavior.

CHAPTER 1. GENERAL INTRODUCTION

Overview

The optical detection and spectroscopy of fluorescent molecules has become a fundamental and versatile tool in research of physical, chemical and biological problems. Specifically, site-selective excitation and line-narrowing techniques, which probe only a subset of impurity molecules and provide more informative and sensitive material response, have been of particular interest. For example, the study of chlorophylls by hole burning spectroscopy sheds light on the understanding of pathways of complicated energy and charge transfer processes in photosynthesis.[1-18] Hole burning properties of rhodamine 800 molecules indicate differences between carcinoma cells and normal cells.[19-21] Various line-narrowing techniques can be used to probe molecular properties.[22, 23] Among them, single molecule spectroscopy is the ultimate line-narrowing technique which allows the study of exactly one single molecule and uncovers individual molecular characteristics hidden under the ensemble average.[24-41] On the other hand, the advancement of time-domain techniques has allowed researchers to study molecular dynamics within femtoseconds, which pertains to the time scale of making and breaking of chemical bonds.[42,43] For instance, the dynamics of intramolecular vibrational energy redistribution can be monitored by using ultrafast pump-probe laser spectroscopy,[42] and even the results of a chemical reaction with two different channels can be controlled by selective vibrational excitation.[44] While the photophysical properties of single molecules are revealed by single molecule spectroscopy, the study of the reaction kinetics of individual biomolecules reactivity can lead to an understanding between structure and inherently heterogeneous reactivity of enzymes.[45-52]

In this dissertation, many different laser-based techniques are used to investigate molecular activity. Hole burning and single molecule spectroscopy are used to study the energy transfer properties of the red antenna states of cyanobacterium photosystem I (CHAPTERS 2 & 3). A variant of time-resolved coherent anti-Stokes Raman spectroscopy is used to monitor the evolution of vibrational modes of coumarin 153 in the electronic excited state (CHAPTER 4). The last chapter of this dissertation presents a study of the reaction rates of individual alkaline phosphatase molecules in liposomes by laser-induced fluorescence and microscopy.

Part I.

Introduction to Hole Burning, Single Molecule Spectroscopy and Red Antenna States of Cyanobacterial Photosystem I

The Lineshape of a Single Impurity Molecule in a Low Temperature Solid Matrix

If temperature is absolute zero (0 K), the linewidth of electronic transition of a chromophore (impurity) in a solid state matrix, $\Gamma(0)$, is given by:[53]

$$\Gamma(0) = \frac{1}{2\pi c \tau_1(0)} \qquad \text{(I.1)}$$

where c is the speed of light and $\tau_1(0)$ is the decay time of the excited state of the chromophore at 0 K. At $T = 0$, the homogeneous linewidth is only a function of the excited state lifetime. The homogeneous lineshape, also known as zero-phonon line (ZPL), is Lorentzian. As temperature increases, the lifetime of the state decreases and the line starts to broaden due to dephasing processes induced by thermally activated phonon modes

in the matrix. When $T > 0$, Γ(T) is governed by excited state lifetime and phase relaxation time:[53]

$$\Gamma(T) = \frac{1}{2\pi c \tau_2(T)} = \frac{1}{\pi c}\left[\frac{1}{2\tau_1(T)} + \frac{1}{\tau_2^*(T)}\right] \quad \text{(I.2)}$$

where $\tau_2(T)$ is the dephasing time and $\tau_2^*(T)$ is the phase relaxation (pure dephasing) time at T K. Quite frequently, the temperature dependence of τ_1 is insignificant as compared to τ_2^* and can be neglected. The τ_2^* is the time of the time-dependent part of the excited state wavefunction change from $\exp(iE_{ex}t/\hbar)$ to $\exp[i(E_{ex}t/\hbar+\delta)]$. One should note that τ_2^* approaches infinity if the molecule is imbedded in a crystal of 0 K. One the other hand if the glassy matrix temperature is above 3-4 K, τ_2^* decreases dramatically and second term starts to dominate.[53]

Analogous to the vibronic states of molecules in gas phase, vibrational modes of solid lattices, phonons, also couple to electronic transition of guest molecules and that interaction is called electron-phonon coupling. Fig. I.1 illustrates strong and weak cases of the electron-phonon coupling and their corresponding absorption spectra. When the electron-phonon coupling is weak, the main feature of the absorption spectrum is the ZPL, along with a small phonon sideband (PSB).[23] When the electron-phonon coupling is large, the PSB becomes significant compared to the ZPL. The structure and width of PSB depend on local lattice dynamics at the impurity center, the electron-phonon coupling, and temperature.[53] The relative strength of the ZPL and the PSB can be explained by the Franck-Condon principle. In Fig. I.1a, the impurity molecule has a small change of geometry during the electronic excitation which can be approximated by a vertical transition, and the electron-phonon coupling is relatively small, leading to a weak PSB in the absorption spectrum. On the other hand, for the case of strong electron-phonon

coupling (Fig.I.1b), the molecule goes through a large change of geometry during the electronic excitation and therefore a strong PSB appears in the spectrum.

The spectral intensity of ZPL and PSB can be characterized by the Debye-Waller factor (DWF), α (also known as FC factor):[53]

$$\alpha = \frac{I_{\mathrm{ZPL}}}{I_{\mathrm{ZPL}} + I_{\mathrm{PSB}}} \tag{I.3}$$

where I_{ZPL} and I_{PSB} are the integrated intensities of ZPL and the PSB, respectively. In the harmonic oscillator model at $T \sim 0$ for N phonon modes, the DWF factor is given by:[53]

$$\alpha = \exp(-S) \tag{I.4}$$

where S is the Huang-Rhys factor and can be described by:[53]

$$S(T=0) = \frac{M_i \omega_i}{2\hbar} \sum_i (\Delta q_i)^2 \tag{I.5}$$

In Eq. I.5, M and ω_i are the reduced mass and frequency of the phonon mode i, respectively, and Δq_i is the change of the equilibrium position corresponding to the lattice normal coordinate q_i. From Eq. I.5, we can see that $S \propto (\Delta q_i)^2$. Thus, S can be used to characterize the strength of the electron-phonon coupling. In general, the electron-phonon coupling is weak when $S < 1$. For $S > 1$, the electron-phonon coupling is strong.[53]

Both local lattice dynamics and the strength of the PSB are temperature-dependent, and so is the DWF. The temperature dependent DWF is given by:[53]

$$\alpha(T) = \exp\left[-\sum_i^N S(2\bar{n}_i + 1) \right] \tag{I.6}$$

where thermal occupation number, $\bar{n}_i = \left[\exp(\hbar\omega_i / kT) - 1\right]^{-1}$, is the average number of phonons of mode i at temperature T. $\alpha(T)$ reaches its maximum value at very low temperatures (T $\leq$ 10 K for most organic glasses).

Inhomogeneous Broadening

Ideally, each dye molecule in a perfect crystal has the same immediate local environment and transition frequency; so that the homogeneous lineshape of the electronic transition can be described by a single ZPL (see Fig. 2a). For example, such impurity lines are observed in Shpols'kii matrices, which are microcrystalline matrices of alkanes such as hexane, octane, and etc. However, even very small differences in the local environment of the impurity may cause a large frequency shift in its absorption (see Fig. 2b). This leads to the phenomenon of inhomogeneous broadening, where the homogeneous ZPLs are buried in the ensemble of transition frequencies of molecules.

In general, inhomogeneous broadening is referred to the statistical distribution of the single site absorption spectra and can be characterized by an inhomogeneous distribution function (IDF), $G(\omega)$, which is usually a Gaussian profile with a full width at half maximum of Γ_{inh}.[53] Therefore, the absorption spectrum for the ensemble of the chromophores is the convolution of single site absorption spectra (including the ZPL and PSB) and the distribution function of these sites. The Γ_{inh} is usually significantly larger than the homogeneous linewidth, $\Gamma(0)$. For example, for molecules in glasses or proteins matrices, the Γ_{inh} is around 100-400 cm^{-1} and $\Gamma(0)$ is ~0.0001 cm^{-1}. But, even for molecules in Shpol'skii systems, the Γ_{inh} is around 1-5 cm^{-1}, which is still 3-4 orders greater than $\Gamma(0)$.

Several spectroscopic techniques of selective excitation at low temperature such as fluorescence line narrowing,[22,23] spectral hole burning (SHB),[1-18,22,53,54] and single molecule spectroscopy (SMS)[24-41] have been developed to unearth ZPLs obscured by inhomogeneous broadening. A common property of these techniques is that they are typically low

temperature techniques. This is because, first, Γ_{inh} depends on temperature only very weakly for a given solid substance and second, according to Eqs. I.2 and the I.3. the lower the temperature is, the narrower the ZPL is and the higher the ZPL amplitude compared to PSB amplitude is. Thus, low temperature maximizes these line-narrowing techniques' resolution limit – the ratio of $\Gamma_{inh}/\Gamma(T)$.

Spectral Hole Burning

If a molecule relaxes back to its original ground state after electronic excitation, then the transition frequency of this molecule remains the same. Nevertheless, in certain substances, a small fraction of excited molecules may be subject to photochemical or nonphotochemical transformation and not return to the same ground state. As a result, a spectral hole appears in the absorption spectrum and this process is called spectral hole burning (SHB). A spectral hole can fill as soon as burning light stops – such holes are called transient; if holes can be observed (at least few seconds) after the burning light is turned off, they are called persistent spectral holes. In photochemical hole burning (PHB), the hole formation occurs due to light-induced chemical reactions such as tautomerization, isomerization, or bond breaking. In the case of nonphotochemical hole burning (NPHB), a fraction of excited molecules activate a rearrangement of solid matrix around them, leading to the change of transition frequencies and spectral holes. A typical reason for the observation of a transient hole (a.k.a. population bottleneck hole) is possibility in some systems to pump impurity molecules into long-lived state (usually a triplet state), which does not absorb resonant light. Transient hole burning is a useful tool in studies of complex photosystems,[14] however it is out of scope for this dissertation.

To observe a spectral hole, four general conditions are necessary: First, the absorption spectrum must be inhomogenously broadened. Second, a light-induced frequency change mechanism must exist. Third, a burning light source must have a narrower linewidth than inhomogeneous broadening. Fourth, the hole filling processes must be slower than the hole burning processes. The latter condition is one of the reasons why SHB is usually performed at liquid helium temperatures and hole burning is limited to temperatures, $T < 130$ K.[22,53]

The energy landscape in low temperature amorphous system is usually very complicated. The frequency change mechanism in persistent spectral hole burning (PSHB) is commonly explained with the help of two level systems (TLS) (see Fig. I.3a). In the TLS model, hole burning occurs as the following. Initially, the molecule is trapped in the left well of the ground state (g) of the TLS. Then excitation with the burn frequency ω_b brings a molecule to the electronically excited level (e) in the left well. Next, the tunneling takes place in the excited state and finally, the molecule relaxes back to the right well and emits a photon of frequency ω_2, which is different from ω_b. In amorphous matrices, there are two types of TLS – extrinsic, TLS_{ext} and intrinsic, TLS_{int}. The TLS_{int} of the host matrix are intimately connected with excess free volume; TLS_{ext} are closely related to the impurity molecules and therefore associated with impurity and host molecules in the nearest neighborhood. While TLS_{ext} are responsible for the frequency change in hole burning, TLS_{int} determine the dynamic features of the zero phonon hole (ZPH) such as its width and dephasing properties.

A hole burning spectrum can be obtained by subtracting the pre-burn spectrum from the post-burn spectrum. The spectrum of hole burning usually consists of more spectral

features than the ZPH. On the high-energy side of the ZPH, a phonon side band hole (PSBH) can be observed. The amplitude of the PSBH is proportional to that of PSB in the single site absorption spectrum; however, it may be invisible due to its low amplitude in weakly electron-phonon coupled systems. On the low-energy side of the ZPH, a pseudo-PSBH can be observed frequently – this hole appears because some molecules absorb ω_B through their phonons in the electronically excited state. In addition to phononic excitation, vibronic excitation is also possible. These vibronically excited molecules rapidly relax back to the zero vibrational level in their excited states. After hole burning takes place, these sites lose absorption at frequency of $\omega_A = \omega_B - \nu$, where ν is the vibrational frequency. Consequently, a satellite hole appears at ω_A along with the ZPH at ω_B.

Hole burning is a dynamic process; different burn fluences result in different spectral features. At low intensities only the ZPH forms; at medium intensities both the ZPH and PSBH become observable. At very high intensities, spectral features may merge and complicated energy landscape may introduce new hole burning channels, which can make initial spectrum quite unrecognizable.[10]

Mechanism of NPHB. In 1978, Hayes and Small proposed the first mechanism of NPHB based on a static distribution of extrinsic two-level systems (TLS_{ext}) to explain the frequency change in persistent nonphotochemical hole burning.[54] A scheme of transitions of TLS coupled to the impurity molecule is shown in Fig. I.3a. The superscripts g and e stand for the ground and excited states of the impurity. After electronic excitation by laser frequency ω_B, the originally trapped chromophore in the left well converts to the right well and remains there during relaxation. In the late 1980s, results from optical dephasing studies showed that NPHB could not be fully explained by the static distribution model of

TLS_{ext}.[55] They suggested that not only TLS_{ext} but TLS_{int} plays an important part in NPHB. Later, Shu and Small proposed that NPHB is the result of a hierarchy of tunneling events triggered by optical excitation.[55-56] First, the electronically excited molecule creates a wide perturbation in both the inner and outer shell of local spheres. The perturbation then triggers a faster relaxation of the TLS_{int} in the outer shell and terminates in the inner shell where the rate determining step involving the TLS_{ext} occurs. The second step results in diffusion of excess free volume from the outer shell to the inner shell of the impurity and this out-side-in process of the matrix rearrangement leads to change of absorption frequency and hole formation.

The model of TLS_{ext} describes well the behaviors of NPHB at low burning fluences, however, it does not provide a good approximation to the hole burning process at higher fluences due to various saturation effects.[10] In the theoretical model based on TLS_{ext}, hole growth slows down at medium fluences and finally stops; experimental observations are that ZPH and pseudo PSBH continue to grow indefinitely.[10] In order to resolve this discrepancy, an additional second channel was introduced to the TLS_{ext}, which results in extrinsic multilevel systems (MLS_{ext}), and is shown in the Fig. I.3b.[10] MLS_{ext} can be considered as additional parallel hole burning channels with different tunneling rates that are located on the same guest molecule. At high burning intensities, some guest molecules are brought to the "trap states" of the MLS_{ext} (the right most well of Fig. I.3b) and become spectrally inaccessible by the laser frequency due to dramatic change of the transition energy.

Applications of NPHB. If the hole burning process was related only to impurity molecule, then one would not expect hole burning to reflect any property or information

regarding the change of the host matrix. Instead, the mechanism of NPHB requires that large number of TLS_{int} must participate in hole burning. In other words, the impurity molecule and the host matrix become coupled in the process of NPHB, thus allowing NPHB to probe the local environment of the guest molecules. On the other hand, spectral holes can be extremely narrow – up to 10^8 times narrower than inhomogeneous broadening. Consider that if some external field (e.g. electric or pressure) changes the chromophore resonance frequency, then the sharper the hole is, the smaller the change that can be detected. Examples of typical NPHB applications include: Measurement of ZPH widths, which allows determining excited state lifetimes, excitation energy transfer rates, and optical dephasing times. Temperature dependence of ZPH widths reveals dephasing mechanism(s), which may include coupling with phonons, librons, TLSs and local modes. Hole shape and hole-growth kinetics provide electron-phonon coupling parameters, shed light on dephasing mechanism, and on structural heterogeneity. Inhomogeneous broadening and site distribution function can be obtained by action spectra. In Stark hole burning experiments, the phenomena of hole broadening and splitting can be used to measure the permanent dipole moment change, which is closely related to strongly couple molecules and their corresponding charge transfer character. From high-pressure hole burning spectroscopy, the linear pressure-shift rates of ZPH can be found, and used to identify closely spaced excited states that cannot be easily resolved by other hole burning techniques.

Single Molecule Spectroscopy

The optical detection and spectroscopy of a single molecule was first reported in the late 1980s.[24] By using sensitive double-modulation techniques, single pentacene molecules in a *p*-terphenyl crystal were observed at liquid-helium temperature.[24] Later, the same impurity-host system was used to obtain fluorescence excitation spectra of the single molecules.[25] The greatly improved signal-to-noise ratio of the fluorescence signal opened gates for many experiments.[39] For example, the lifetime-limited homogeneous linewidth of a single molecule has been measured down to a resolution of a few MHz.[25,31] Spectral landscapes have also been observed by scanning the laser focal spot across the solid surface.[28] The resulting three dimensional image offers spatial separation, spectral resolution and fluorescence intensity of individual peaks of single molecules. Further, combining with confocal microscopy, single molecule experiments provide good signal-to-noise ratio comparable to near-field optical scanning microscopy.[33,34,59] The marriage of the two techniques made SMS a powerful tool in areas of applications and widely accessible to many research groups.[39] For those more interested, several excellent reviews of SMS can be found in ref. 39-41 and 60.

Requirements of SMS. Two requirements are important to achieve SMS. First, only one molecule should be in resonance in the probing volume of laser. Second, the signal-to-noise ratio (SNR) should be as large as possible.[31,40,41]

For room temperature experiments, one molecule in resonance can be guaranteed by using highly diluted solutions. For a probing volume of 10 μm^3, a solution in the concentration range of 10^{-10} M should be used in single molecule detection.[40] On the other hand, more concentrated samples (4~5 orders higher) can be used in low temperature

experiments by tuning the laser frequency to the edge of inhomogeneous broadening of the absorption spectrum.[40]

The SNR for single molecule detection by fluorescence excitation can be approximated by:[31, 41]

$$\mathrm{SNR} = \frac{D\phi_F \sigma P_0 \tau / Ah\nu}{\sqrt{\frac{\left(D\phi_F \sigma^P P_0 \tau\right)}{Ah\nu} + C_b P_0 \tau + N_d \tau}} \qquad \text{(I.7)}$$

where D (= $\eta_Q F_p F_f F_l$) describes the overall efficiency for the detection of emitted photons (where η_Q is the quantum efficiency of the photodetector, F_p is the fraction of the total emission solid angle collected by the objective, F_f is the fraction of emitted fluorescence which passes through the low-pass filter and F_l is the total transmission of the windows and collection optics along the way to the photodetector), ϕ_F is the fluorescence quantum yield, σ is the peak absorption cross-section, P_0 is the laser power, τ is the integration time, A is the focal spot area, $h\nu$ is the exciting photon energy, C_b is the background count rate, and N_d is the dark count rate. The numerator is the peak detected fluorescence from one molecule in an interval of time τ, and the three terms in the denominator represent shot noise contributions from the emitted fluorescence, background, and dark signal, respectively.[31,41] According to Eq. I.7, several important requirements need to be met in order to provide optimum SNR for SMS. First, one should minimize the probe volume to suppress the background signal. Additionally, several molecular properties are also important to SMS: the molecule should have a large peak absorption cross-section, high photostability, high fluorescence quantum yield, weak bottlenecks into triplet states, and the molecule should operate below the saturation of molecular absorption.[31,41]

Applications of SMS. Several physical phenomena in low temperature have been observed for first time by SMS. For example, light-induced spectral shifting and spectral diffusion of a single molecules due to conformational changes of the molecule's nanoenvironment were reported.[27] Studies of photon antibunching in single molecule systems revealed the changes in the triplet yield and triplet state lifetime of single molecules.[61] In addition, vibrational modes of single molecules in crystals and polymers were also resolved by the emission spectra of single molecules.[62,63]

Techniques of single molecule detection and spectroscopy have also been applied to biological systems, which are traditionally investigated by various modes of microscopy. For instance, precise measurement of molecular positions provide the rate of translational diffusion.[64] Monitoring the emission from the enzyme's fluorescent active site reveals the dynamics of enzymatic turnovers in real time.[49] By combining appropriate fluorophores and the Förster resonance energy transfer techniques, one can monitor real-time DNA cleavage, repair and hybridization by restriction enzymes.[60,65,66]

Single molecule spectroscopy also provides insight to biophysical properties of photosynthesis. Individual pigment-protein complexes of purple bacteria have been studied by single molecule spectroscopic techniques.[67-70] The observation of energy localization in one band and energy delocalization over the other band of individual photosynthetic complexes of purple bacteria provides important information for exciton model and excitation energy calculation.[69,70] For photosystem I of the cyanobacterium *Synechococcus elongatus*, fluorescence emission spectra of two antenna states of single complex show that they are different not only in the spectral location but also in their strength of electron-phonon coupling.[67,68]

Red Antenna States of PSI of Cyanobacteria

Photosynthesis, the most important process of storing solar energy on earth, is usually expressed by the deceptively simple chemical equation:

$$6\ H_2O + 6\ CO_2 \rightarrow 6\ O_2 + C_6H_{12}O_6 \qquad (I.8)$$

In fact, the photosynthetic process is a sophisticated series of redox reactions driven by sunlight.[71,72] Two coupled membrane protein complexes named photosystems I and II (PSI and PSII) in green plants, green algae, and cyanobacteria are responsible for the major reactions of photosynthesis. The chemical reactions of PSI and PSII are interlinked by a chain of electron carriers. The primary product of PSI is carbohydrates and the primary products of PSII are ATP and oxygen.[71,72]

Much attention to PSI is stimulated by the 2.5Å resolution X-ray structure of PSI of cyanobacterium.[71,72] The PSI of cyanobacterium exists as a trimer while it is a monomer for higher plants. The major function of the PSI protein complex is to convert photons into chemical energy by transferring electrons from plastocyanin/cytochrome C_6 on the luminal side to ferredoxin/flavodoxin at the stromal side of membrane. Each monomer consists of 12 protein subunits, a complicated network of chlorophyll *a* (Chl *a*) molecules, 22 carotenoids, 3 [4Fe4S] clusters and 2 phylloquinones.[71,72] Despite that the high resolution X-ray structure of PSI (from thecyanobacterium *Synechococcus elongates*) is available,[71,72] the connection between structure and spectrum remains undetermined. The seemingly unorganized chl *a* network contains a strongly coupled special pair of reaction center (RC), P700, 4 Chls for electron transfer and ~90 antenna Chl *a* molecules.[71,72] In addition to the major antenna states located at ~680 nm, there are antenna states that absorb at energies lower than P700*, the primary electron donor state of the RC. According to the crystal

structure and spectroscopic data of PSI, dimers and trimers of chlorophylls are responsible for these red-absorbing antenna states.[10,71,72] The major function of the red antenna states of PSI is well known: these red states can transfer energy upward to RC at physiological temperature and, further, they can also trap energy from higher antenna states as a role of photoprotector.[73] Thus they are very important in the functioning of PSI. For more details regarding the red states of PSI, ref. 9-11, 71, 72 are suggested.

Research Objectives

The red antenna states of PSI are known to originate from closely spaced Chls *a* that contain strong charge transfer character. According to theoretical simulation[57] and previous experimental results[74] on photosynthetic complexes, hole splitting behavior should be observed by Stark HB experiments when chromophores possess strong charge transfer character. Therefore, our goal was to apply high-resolution Stark HB techniques to study these chlorophyll molecular aggregates in the red antenna states of PSI. On the other hand, previous NPHB results showed that more than one red antenna state or chl aggregate is responsible for the absorption spectrum of the red antenna band.[9-11,74] Our second objective was to use NPHB and SMS to examine the energy transfer characters between high energy red antenna states and low energy ones and to determine the corresponding energy transfer rate of these states.

Part II

Introduction to Coherent Anti-Stokes Raman Spectroscopy

Coherent anti-Stokes Raman scattering (CARS) is a nonlinear four wave mixing (FWM) process. The interaction between matter and electric fields may be expressed as a power series in the applied electric field:

$$\vec{P} = \chi^{(1)} \cdot \vec{E} + \chi^{(2)} : \vec{E}\vec{E} + \chi^{(3)} \vdots \vec{E}\vec{E}\vec{E} + ... \quad \text{(II.1)}$$

where the vector $\vec{P}$ is the macroscopic polarization vector, χ is the dielectric susceptibility, and the vector $\vec{E}$ is the electric field. Under low intensity of applied electric field, only the first order term is important. This linear term describes linear optical effects like absorption, refraction, Rayleigh scattering, and normal Raman Scattering. When the strength of the fields approaches high levels, nonlinear terms become important. The first nonlinear term is responsible for frequency doubling ($2\omega_1$), sum frequency generation ($\omega_1 + \omega_2$) and difference frequency generation ($\omega_1 - \omega_2$) observed in crystals. For liquids and gases this term is zero due to their isotropy. The third term is always present in all materials and responsible for frequency combination of three waves, for example ($3\omega_1$), ($\omega_1 + \omega_2 + \omega_3$), ($2\omega_1 + \omega_2$), and ($\omega_1 - \omega_2 + \omega_3$). The last one represents the CARS process (see Fig II.1).

The advantages of CARS spectroscopy over spontaneous Raman spectroscopy are the high intensity emission and the separation from fluorescence signal. Typically, CARS signal is many orders of magnitude stronger than conventional Raman scattering. Second the CARS signals are coherent and therefore all the CARS signals can be collected.

Compared to an isotropic, incoherent scattering or emission process with ~1% collection efficiency, this coherency leads to a small solid angle of CARS emission and ~100% collection efficiency of CARS radiation, which strongly reduces undesirable backgrounds such as fluorescence. As a consequence, CARS provides a high signal-to-interference ratio and is capable of probing molecules in high background environments over a broad range of experiment conditions.

Magnitude and Phase-Matching Requirement of CARS. The theory of CARS is well known and several excellent reviews give the theoretical background of CARS.[75-84] Here, we will only introduce important equations in the CARS theory.

Assuming that the CARS process involves plane and monochromatic waves, the equation of electric field is represented as:

$$\vec{E}(z,t) = \sum_{m=1}^{4} \vec{E}_m \exp(-i\omega_m t + i\vec{k}_m \vec{z}) + \vec{E}_m^* \exp(i\omega_m - i\vec{k}_m \vec{z}) \qquad \text{(II.2)}$$

By using Maxwell's equations and the constitutive relationship of polarization and electric field, one can derive the nonlinear wave equation of the propagation of light in a medium as:[83,84]

$$\Delta\vec{E} = \frac{n^2}{c^2}\frac{\partial\vec{E}}{\partial t^2} + \frac{4\pi}{c^2}\frac{\partial\vec{P}_4}{\partial t^2} + \frac{4\pi}{c^2}\sigma\frac{\partial\vec{E}}{\partial t} \qquad \text{(II.3)}$$

where $\vec{E}$ is the electric field of the light wave, n is the refractive index, c is the speed of light, and $\vec{P}_4$ is the nonlinear polarization of the medium. Eq. II.3 represents the interaction of incoming waves and the medium, which generates a new wave with polarization $\vec{P}_4$. Utilizing notations similar to Eq. II.2, the electric field and polarization can be written as $E = \frac{1}{2}[E_4(\omega_4, z)\exp(ikz - \omega_4 t) + c.c.]$ and $P = \frac{1}{2}[P^{(3)}(\omega_4, z)\exp(ikz - \omega_4 t) + c.c.]$; then by

substituting these notations into Eq. II.3 and assuming that the magnitude of the electric field changes slowly along the z direction, one can obtain the basic gain equation:[78,83]

$$dE(\omega_4, z) = \frac{2\pi i \omega_4}{n_4 c} P^{(3)}(\omega_4, z) dz \tag{II.4}$$

Further, the intensity of the generated CARS signal along the z direction can be obtained by integrating Eq. II.4 over the range from z = 0 to z = l: [82]

$$I_{CARS} = \frac{\omega_{CARS}^2}{n_1 n_2 n_3 n_4 c^4 \varepsilon_0^2} \left|\chi_{CARS}\right|^2 I_1 I_2 I_3 l^2 \left[\frac{\sin(\frac{\Delta k l}{2})}{\frac{\Delta k l}{2}}\right] \tag{II.5}$$

where I is the intensity of the incident beam, n is the refractive index, ε_0 is the permittivity of free space, l is the length of interaction, χ_{CARS} is the third order nonlinear susceptibility of the medium, and Δk is the magnitude of the wave vector sum of the interacting beams ($\Delta \vec{k} = \vec{k}_1 - \vec{k}_2 + \vec{k}_3 - \vec{k}_{CARS}$).

As one can see in Eq. II.5, the CARS process exists only when incident laser beams are aligned and phased properly. The maximum intensity of the CARS beam occurs when $\vec{k}_{CARS} = \vec{k}_1 - \vec{k}_2 + \vec{k}_3$ (i.e. $\Delta \vec{k}$ =0). This relationship is generally known as the phase-matching requirement of CARS (see Fig. II.2a). There are several approaches for CARS phase matching, as several geometries of the three beams can satisfy phase-matching requirement. They can be collinear CARS, BoxCARS, and folded BoxCARS. Among these geometries, the folded BoxCARS is mostly chosen. In this geometry, three incident beams come from three corners of an imaginary square. After intersecting in the probed medium, three beams and the resultant CARS signal form another imaginary square on the reverse side of the medium (see Fig. II.2b). As a consequence, the folded BoxCARS geometry provides the optimal spatial resolution and separation of the CARS signal beam.

Time-Resolved CARS. By using ultrashort pulses of laser in CARS spectroscopy, important information, such as modes of vibrations, of atoms or molecules can be extracted from the response of the coherently excited systems. In order to explain the relationship between the third-order non-linear polarization of the medium and the Raman-active vibrations, it is convenient to express the nonlinear part of Eq. II.1 as:[81]

$$P_{nl}^{(3)} = \chi^{(3)} E_1 E_2^* E_3 = \frac{N}{4MD}\left(\frac{\partial \alpha}{\partial Q(t)}\right)_0^2 E_1 E_2^* E_3 \qquad \text{(II.6)}$$

where N is the number density of molecules, M is the reduced mass of a molecule, D is a function of the frequency Ω of a Raman active vibration, frequencies of incident waves and a phenomenological damping constant, α is the linear electron polarizability, and Q(t) is the amplitude of the coherent Raman-active molecular vibration. Evident from Eq. II.6, changing incident pulses properties, such as pulse duration and delay time between pump and probe pulses, will alter the result of CARS signal (which is proportional to square of $P_{nl}^{(3)}$) and therefore provide information of the vibrational modes of a molecule.

The development of time resolved (tr)-CARS was stimulated by the advancement of high-power ultrafast lasers as picosecond pulses allowed instantaneous excitation of Raman-active vibrations and measurements of the decay kinetics of the coherent molecular vibrations. Time-domain CARS technique has also been used to study various processes such as dephasing measurements of separate multipole moments of atoms, thereby revealing the nature of dephasing in atomic vapors and determining the relevant dephasing rate.[81] Additionally, recent advancement of femtosecond lasers provides a broad spectral range to probe molecular vibrations simultaneously by detecting the beats of the CARS signal (see Fig. II.3) and therefore allowing one to measure the dynamics of wavepackets in both ground state and excited state molecules.[81]

Research Objective

Conventional femtosecond tr-CARS utilizes three broadband laser pulses to prepare vibrational (or rotational) excited states of molecules by the first two pulses and probe the decay of the beats between vibrations (or rotations) by the third pulse (see Fig. II.3a).[85-90] The oscillations in the measured CARS signal can be later converted by Fourier transform into beat frequencies of the vibrational modes, $|\nu_1 - \nu_2| = \Delta\nu$ (see Fig. II.3b). By changing the delay of laser pulses, the dynamics of vibrational energy transfer can be observed by monitoring these beats. However, this technique can only provide indirect frequency information, Δν, and it is very challenging to find all the origins of the Δν values when several modes of vibration are present in the spectral range of $|\omega_1 - \omega_2|$ (up to $\frac{n(n-1)}{2}$ beat frequencies can originate from n vibrational modes). Further, if one wants to study dynamics of vibrations of excited state molecules by using conventional tr-CARS, it is very difficult since few molecules are fully characterized in terms of their vibrations in the electronic excited state.

By changing the broadband probe beam (a femtosecond pulse) into a narrowband picosecond duration beam in the femtosecond tr-CARS technique, we were able to observe molecular vibrations directly without Fourier transform. Our goal was to detect vibrations of excited state molecule by first pumping the molecules into their excited state and probing them by this fs/ps CARS technique.

Part III

Single Enzyme Reactions in Biomimetic Containers−Liposomes

Enzymatic Reactions of Single Molecules

Reactivity of individual enzyme molecules was first reported in the mid 1990s.[46] Yeung and coworkers used the lactate hydrogenase (LDH-1) solution with very low concentration in a narrow capillary to ensure that only one molecule presents in every discrete zone of the capillary. After individual LDH-1 molecules were reacted with nicotinamide adenine dinucleotide and lactate molecules, the products, NADH, were produced. These fluorescent products were then separated from the enzyme molecules by electrophoresis and probed by laser-induced fluorescence. The broad distribution of reactivity suggested that there are several conformers for this LDH-1 enzyme. This technique was later used to study the activity of different single enzymes such as individual alkaline phosphatase molecules.[48,91] However, capillary is not the perfect reactor for single enzyme reactions since proteins are known to exhibit strong adsorption to the wall of glass.[92] To mimic the biochemical reactions in cellular environment, glass/capillary reactors may not be able to provide a suitable condition.

Liposomes

Liposomes, also known as artificial cells and artificial membranous lipid vesicles, are composed of phospholipid bilayer membranes which provide confined and isolated space for intracellular aqueous solutions (see Fig. III.1). Therefore, the structure of liposomes highly resembles to the structure of living cell membranes, which are composed

of lipid bilayers and types of functional proteins. Both natural (mixed) lipids and synthesized (pure) lipids can be used to prepare various functional liposomes of neutral, positive, and negative charges. This unique property makes liposomes perfect model systems in many areas ranging from fundamental research of molecular biology to novel methods of drug delivery in the pharmaceutical industry.[93] Nevertheless, there was one major disadvantage in liposome research and applications: time-consuming and labor-intensive procedures of liposome synthesis.[94] These tedious procedures usually took several hours to days, especially for preparation of giant liposomes (diameter greater than one micron).[93,94] Fortunately, a rapid rotary evaporative method was invented and allows preparation of giant liposomes in just 2~3 minutes.[93] This novel approach opens the way for many biomolecular applications, especially for highly labile and reactive species. Several chemical and biochemical reactions have been demonstrated by using the liposome reactors. For instance, intercalation of dyes and DNAs,[95] enzymatic reactions,[92,96] and hydrogel formation of polymers and metal ions[97] have been reported. Three major micro-manipulation techniques have also been developed to handle these ultrasmall vesicles in microscopic scale: electrofusion,[95,98,99] electroinjection[92,96,97] and light-induced fusion.[100] To study the kinetics of single protein reactions, electroinjection is probably not a good choice due to the strong adsorption interaction between proteins and the interior glass wall of pulled microneedles. On the other hand, light-induced fusion requires two IR laser for optical trapping and one UV laser for liposome fusion.[100] One major drawback of this technique is the UV laser can potentially damage the protein[101,102] and therefore the activity of individual enzymes.

Research Objectives

In order to eliminate any potential influences from surfaces, orientations and steric effects, the reaction of single alkaline phosphatase molecules is studied inside liposomes. The single enzymatic reaction inside liposomes is initiated by electrofusion which does not cause any damage or loss of proteins during the manipulation. Besides, previous single molecule reactions in capillary are based only upon statistical analysis rather than direct observation of single molecules. Our goal was to use fluorescent microscopy to study reactivity of individual proteins in liposome reactors with direct proof of single molecule image in vesicles.

References

1. Wu, H.-M.; Savikhin, S.; Reddy, N. R. S.; Jankowiak, R.; Cogdell, R. J.; Struve, W. S.; Small, G. J. *J. Phys. Chem*. **1996**, *100*, 12022.
2. Wu, H.-M.; Reddy, N. R. S.; Small, G. J. *J. Phys. Chem. B.* **1997,** *101*, 651.
3. Wu, H.-M.; Ratsep, M.; Lee, I.-J.; Cogdell, R. J.; Small, G. J. *J. Phys. Chem. B.* **1997**, *101*, 7654.
4. Oksanen, J. A. I.; Martinsson, P.; Akesson, E.; Hynninen, P. H.; Sundstrom, V. *J. Phys. Chem. A.* **1998**, *102*, 4328.
5. Wu, H.-M.; Small, G. J. *J. Phys. Chem. B*. **1998**, *102*, 888.
6. Oksanen, J. A. I.; Martinsson, P.; Akesson, E.; Hynninen, P. H.; Sundstrom, V. *J. Phys. Chem. A.* **1998,** *102*, 4328.
7. Pieper, J.; Ratsep, M.; Jankowiak, R.; Irrgang, K.-D.; Voigt, J.; Renger, G.; Small, G. J. *J. Phys. Chem. A.* **1999**, *103*, 2412.

8. Jankowiak, R.; Ratsep, M.; Picorel, R.; Seibert, M.; Small, G. J. *J. Phys. Chem. B.* **1999**, *103*, 9759.

9. Ratsep, M., Johnson, T. W., Chitnis, P. R., Small, G. J., *J. Phys. Chem.* B **2000**, 04, 836.

10. Reinot, T.; Zazubovich, V.; Hayes, J. M.; Small, G. J. *J. Phys. Chem. B.* **2001**, *105*, 5083.

11. Zazubovich, V., Matsuzaki, S., Johnson, T. W., Hayes, J. M., Chitnis, P. R., Small, *Chem. Phys.*, **2002**, *275*, 47.

12. Ihalainen, J. A.; Ratsep, M.; Jensen, P. E.; Scheller, H. V.; Croce, R.; Bassi, R.; Korppi-Tommola, J. E. I.; Freiberg, A. *J. Phys. Chem. B.* **2003**, *107*, 9086.

13. Jankowiak, R.; Ratsep, M.; Hayes, J.; Zazubovich, V.; Picorel, R.; Seibert, M.; Small, G. J. *J. Phys. Chem. B.* **2003,** *107*, 2068.

14. Riley, K.; Jankowiak, R.; Ratsep, M.; Small, G. J.; Zazubovich, V. *J. Phys. Chem. B.* **2004,** *108*, 10346.

15. Hsin, T.-M.; Zazubovich, V.; Hayes, J. M.; Small, G. J. *J. Phys. Chem. B.* 2004, *108*, 10515.

16. Hughes, J. L.; Prince, B. J.; Krausz, E.; Smith, P. J.; Pace, R. J.; Riesen, H. *J. Phys. Chem. B.* **2004**, *108*, 10428.

17. Riley, K. J.; Zazubovich, V.; Jankowiak, R. *J. Phys. Chem. B.* **2006,** *110*, 22436.

18. Riley, K. J.; Reinot, T.; Jankowiak, R.; Fromme, P.; Zazubovich, V. *J. Phys. Chem. B.* **2007**, *111*, 286.

19. Walsh, R. J.; Reinot, T. R.; Hayes, J. M.; Kalli, K. R.; Hartmann, L. C.; Small, G. J. *J. Luminesc.* **2002,** *98*, 115.

20. Walsh, R. J.; Reinot, T. R.; Hayes, J. M.; Kalli, K. R.; Hartmann, L. C.; Small, G. J. *Biophys. J*. **2003,** *84*, 1299.

21. Walsh, R. J.; Reinot, T. R.; Hayes, J. M.; Kalli, K. R.; Hartmann, L. C.; Small, G. J. *PNAS* **2003**, *100*, 1685.

22. Moerner, W. E., In *Persistent Spectral Hole Burning: Science and Applications*; Moerner, W. E. Ed.; Springer-Verlag: New York, 1998; Chapter 1.

23. Jankowiak, R., In *Shpol'skii Spectroscopy and Other Site Selection Methods: Applications in Environmental Analysis, Bioanalytical Chemistry, and Chemical Physics*; Gooijer, C.; Ariese, F.; Hofstraat, J. W.; Eds.; John Wiley & Son, Inc., New York, 2000, 235.

24. Moerner, W. E.; Kador, L. *Phys. Re*V. *Lett.* **1989**, *62*, 2535.

25. Orrit, M.; Bernard, J. *Phys. Re*V. *Lett.* **1990**, *65*, 2716.

26. Kador, L.; Horne, D. E.; Moerner, W. E. *J. Phys. Chem.* **1990,** *94*, 1237.

27. Ambrose, W. P.; Moerner, W. E. *Nature* **1991,** *349*, 225.

28. Ambrose, W. P.; Basché, T.; Moerner, W. E. *J. Chem. Phys.* **1991,** *95*, 7150.

29. Ambrose, W. P.; Basché, T.; Moerner, W. E. *J. Lumin.* **1992**, *53*, 62.

30. Basché, T.; Moerner, W. E. *Nature* **1992**, *335*, 355.

31. Moerner, W. E.; Basché, T. *Angew. Chem. Int. Ed. Engl*. **1993**, 32, 457.

32. Köhler, J.; Disselhorst, J. A. J. M.; Donckers, M. C. J. M.; Groenen, E. J. J.; Schmidt, J.; Moerner, W. E.; *Nature* **1993**, *363*, 242.

33. Nie, S.; Chiu, D. T.; Zare, R. N. *Science* **1994**, *266*, 1018.

34. Funatsu, T.; Hanada, Y.; Tokunaga, M.; Saito, K.; Yanagida, T. *Nature* **1995**, *374*, 555.

35. Gammon, D.; Snow, E. S.; Shanabrook, B. V.; Katzer, D. S.; Park,D.; *Science* **1996**, *273*, 87.

36. Dickson, R. M.; Cubitt, A. B.; Tsien, R. Y.; Moerner, W. E. *Nature* **1997**, *388*, 355.

37. Lu, H. P.; Xun, L.; Xie, X. S. *Science* **1998**, *282*, 1877.

38. Moerner, W. E.; Orrit, M. *Science* **1999**, *283*, 1670.

39. Tamarat, P.; Maali, A.; Lounis, B.; Orrit M.; *J. Phys. Chem. A,* **2000,** *104*, 1.

40. Moerner, W. E *J. Phys. Chem. B,* **2002**, *106*, 910.

41. Moerner, W. E. D. P. Fromm *Rev. Sci. Ins.* **2003,** 74, 3597.

42. Zewail, A. H. *Advances in Chemical Physics* **1997**, *101*, 3.

43. Fleming, G. R.; Joo, T.; Cho, M. *Advances in Chemical Physics* **1997**, *101*, 141.

44. Yoon, S.; Holiday, R. J.; Crim, F. F. *J. Chem. Phys.* **2003,** *119*, 4755.

45. Yeung, E. S. *Annu. Rev. Phys. Chem.* **2004**, *55*, 97.

46. Xue, Q.; Yeung, E. S. *Nature* **1995**, *373*, 681.

47. Tan, W.; Yeung, E. S. *Anal. Chem.* **1997**, *69*, 4242-4248.

48. Craig, D. B.; Arriaga, E. A.; Wong, J. C. Y.; Lu, H.; Dovichi, N. J. *J. Am. Chem. Soc.* **1996**, *118*, 5245.

49. Lu, H. P.; Xun, L.; Xie, X. S. *Science* **1998**, *282*, 1877.

50. Li, H.-W.; Yeung, E. S. *Anal. Chem.* **2005**, *77*, 4374.

51. Xu, X.; Yeung, E. S. *Science* **1997**, *275*, 1106.

52. Xu, X.-H.; Yeung, E. S. *Science* **1998**, *281*, 1650.

53. Rebane, K. K.; Rebane, L. A. In *Persistent Spectral Hole Burning: Science and Applications*; Moerner, W. E. Ed.; Springer-Verlag: New York, 1998; Chapter 2.

54. Hayes, J. M., Small, G. J. *Chem. Phys.*, **1978,** *27*, 151.

55. Shu, L., Small, G. J. *Chem. Phys.*, **1990,** *141*, 447.

56. Shu, L., Small, G. J. *Opt. Soc. Am. B*, **1992,** *9*, 724

57. Kohler, M.; Friedrich, J.; Fidy, J. *Biochim. Biophys. Acta* **1998**, *1386*, 255.

58. Kador, L.; Haarer, D.; Personov, R. *J. Chem. Phys*. **1987**, *86*, 5300.

59. Betzig, E; Chichester, R. J. *Science* **1993**, *262*, 1422.

60. Weiss, S. *Science* **1999**, *283*, 1676.

61. Basché, T.; Moerner, W. E.; Orrit, M.; Talon, H. *Phys. Rev. Lett.* **1992**, *69*, 1516.

62. Tchénio, P.; Myers, A. B.; Moerner, W. E. *J. Phys. Chem.* **1993,** *97*, 2491.

63. Tchénio, P.; Myers, A. B.; Moerner, W. E. *Chem. Phys. Lett*. **1993**, *213*, 325.

64. Schutz, G. J.; Trabesinger, W.; Schmidt, Th. *Biophys. J.* **1998**, *74*, 2223.

65. Ha, T.; Enderle, Th.; Ogletree, D F.; Chemla, D. S.; Selvin, P. R.; Weiss, S. *PNAS* **1996**, *93*, 6264.

66. Lebofsky, R.; Bensimon, A. *Briefings in Functional Genomics and Proteomics*, **2003**, *1*, 385.

67. Jelezko, F.; Tietz, C.; Gerken, U.; Wrachtrup, J.; Bittl, R. *J. Phys. Chem. B.* **2000**, *104*, 8093.

68. Tietz, C.; Chekhlov, O.; Drabenstedt, A.; Schuster, J.; Wrachtrup, J. *J. Phys. Chem. B.* **1999,** *103*, 6328.

69. van Oijen, A. M.; Ketelaars, M.; Kohler, J.; Aartsma, T. J.; Schmidt, J. *J. Phys. Chem. B.* **1998**, *102*, 9363.

70. van Oijen, A. M.; Ketelaars, M.; Kohler, J.; Aartsma, T. J.; Schmidt, J. *Science* **1999**, *285*, 400.

71. Jordan, P.; Fromme, P.; Witt, H. T.; Klukas, O.; Saenger, W.; Krauss, N. *Nature* **2001**, *411*, 909.

72. Fromme, P., Jordan, P. and Krauss, N. *Biochim. Biophys. Acta* **2001,** *1507*, 5.

73. Karapetyan, N. V.; Holzwarth, A. R.; Rogner, M. *FEBS Lett*. **1999**, *460*, 395.

74. Ratsep, M.; Wu, H.-M., Hayes, J. M.; Blankenship, R. E.; Cogdell, R. J.; Small, G. J. *J. Phys. Chem*. *B* **1998**, *102*, 4035.

75. Akhmanov, S. A.; Koroteev, N. I.; *Methods of Nonlinear Optics in Light Scattering Spectroscopy* Nauka: Moscow, 1981.

76. Eesley, G. L. *Coherent Raman Spectroscopy*. Pergamon Press: Oxford, 1981.

77. Eckbreth, A. C. *Laser Diagnostics for Combustion Temperature and Species*. Abacus: Cambridge, MA, 1988.

78. Tolles, W. M.; Nibler, J. W.; McDonald, J. R. Harvey, A. B. *Appl. Spectrosc.* **1977**, *31*, 253.

79. Shen, Y. R. *The Principles of Nonlinear Optics*. Wiley: New York, 1984.

80. Reintjes, J. F. *Nonlinear Optical Parametric Processes in Liquids and Gases*. Academic Press: New York, 1984.

81. Zheltikov, A. M. *J. Raman Spectrosc.* **2000,** *31*, 653.

82. Papac, M. J.; Posner, J. D.; Dunn-Rankin, D. *Appl. Spectrosc.* **2003,** *57*, 93.

83. Tolles, W. M.; Harvey, A. B. In *Chemical Application of Nonlinear Raman Spectroscopy*; Harvey, A. B. Ed.; Academic Press: New York; Chapter 1.

84. Mukamel, S. *Principles of Nonlinear Optical Spectroscopy;* Oxford University Press: New York, 1995.

85. Hayden, C. C.; Chandler, D. W. *J. Chem. Phys.* **1995,** *103*, 10465.

86. Lang, T.; Kompa, K.-L.; Motzkus, M *Chem. Phys. Lett.* **1999,** *310*, 65.

87. Felker, P. M.; Zewail, A. H. In *Femtosecond Chemistry*; Manz, J.; Wöste, L. Eds.; VCH: Weinheim, 1995; vol. I.

88. Schmitt, M.; Knopp, G.; Materny, A.; Kiefer, W. *J. Phys. Chem. A* **1998,** *102*, 4059.

89. Knopp, G.; Pinkas, I.; Prior, Y. *J. Raman Spectrosc.* **2000,** *31*, 51.

90. Knopp, G.; Radi, P.; Tulej, M.; Gerber, T.; Beaud, P. *J. Chem. Phys.* **2003,** *118* 8223.

91. Polakowski, R.; Craig, D. B.; Skelley, A.; Dovichi, N. J. *J. Am. Chem. Soc.* **2000**, *122*, 4853.

92. Karlsson, A.; Scott, K.; Markström, M.; Davidson, M.; Konkoli, Z.; Orwar, O. *J. Phys. Chem. B* **2005**, *109*, 1609.

93. Moscho, A.; Orwar, O.; Chiu, D. T.; Modi, B. P.; Zare, R. N. *PNAS* **1996**, *93*, 11443.

94. *Liposomes: A Practical Approach*; Torchilin, V.; Weissig, V. Eds.; Oxford University Press: New York, 1990.

95. Strömberg, A.; Karlsson, A.; Ryttsén, F.; Davidson, M.; Chiu, D. T.; Orwar, O. *Anal. Chem.* **2001**, *73*, 126.

96. Sott, K.; Lobovkina, T.; Lizana, L.; Tokarz, M.; Bauer, B.; Konkoli, Z.; Orwar, O. *Nano Lett.* **2006**, *6*, 209.

97. Jesorka, A.; Markstrom, M.; Orwar, O. *Langmuir* **2005**, *21*, 1230.

98. Chiu, D. T.; Wilson, C.; Ryttsen, F.; Stromberg, A.; Farre, C.; Karlsson, A.; Nordholm, S.; Gaggar, A.; Modi, B. P.; Moscho, A.; Garza-Lopez, R. A.; Orwar, O.; Zare, R. N. *Science* **1999**, *283*, 1892.

99. Chiu, D. T.; Wilson, C. F.; Karlsson, A.; Danielsson, A.; Lundqvist, A.; Stromberg, A.; Ryttsen, F.; Davidson, M.; Nordholm, S.; Orwar, O.; Zare, R. N. *Chem. Phys.* **1999**, *247*, 133.

100. Kulin, S. K.; Kishore, R.; Helmerson, K.; Locascio, L. *Langmuir* 2003, *19*, 8206.

101. Radu, L.; Constantinescu, B.; Gazdaru, D.; Mihailescu, I. *Radiat. Prot. Dosimetry* **2002,** *99*, 153.

102. Lukas, C.; Falck, J.; Bartkova, J.; Bartek, J.; Lukas. J. *Nat. Cell Biol.* **2003,** *5*, 255.

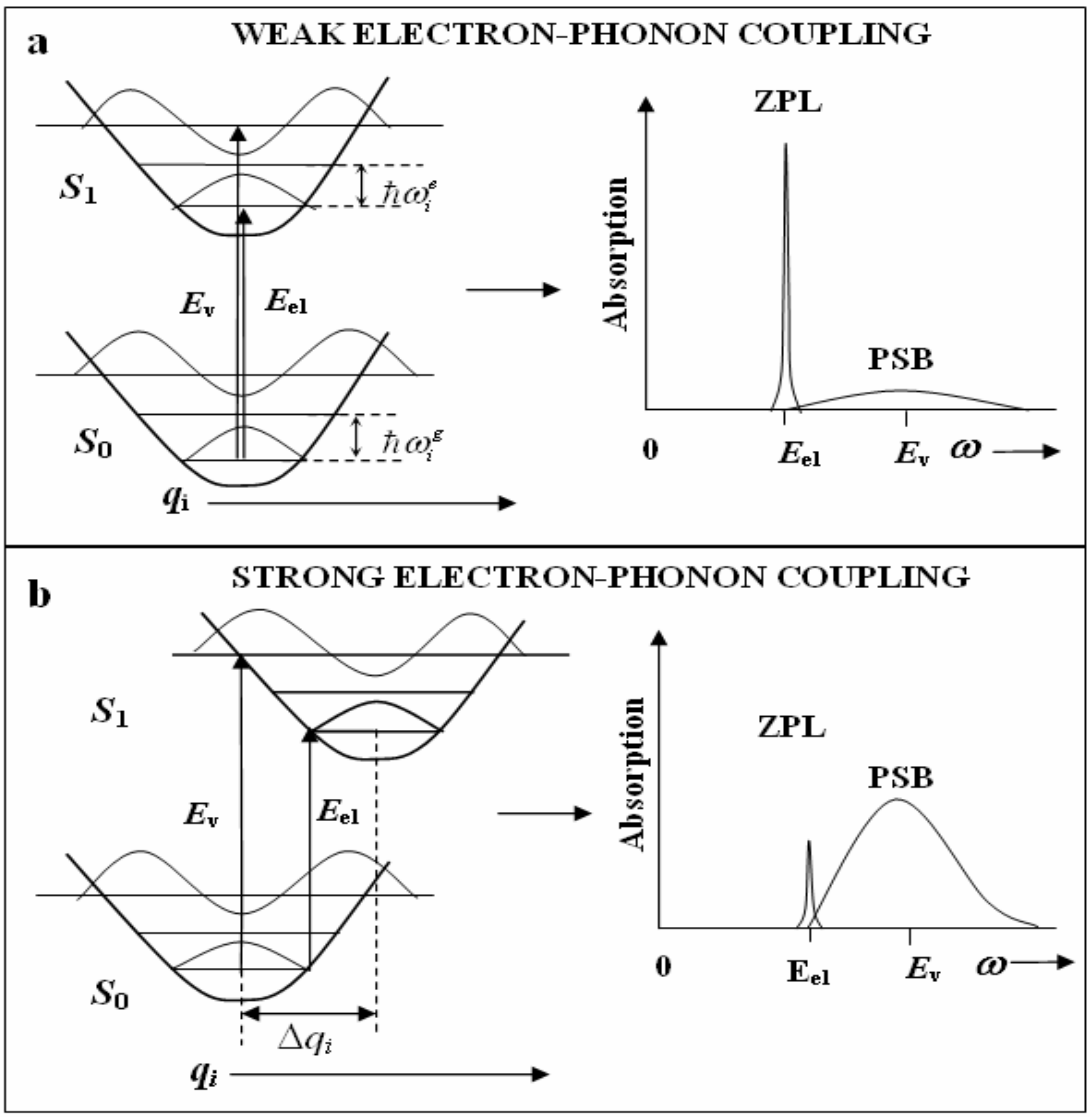

Figure I.1. Schematic presentation of potential energies and corresponding absorption spectra of the electronic transition from the ground state, S_0, to the excited state, S_1, of a guest molecule in a low temperature solid matrix. $\hbar\omega_i^g$ and $\hbar\omega_i^e$ are the corresponding vibrational energy quanta of local phonon mode i in a lattice normal coordinate q_i. **(a)** and **(b)** represent the cases of weak and strong electron-phonon coupling, which correspond to small and large changes of equilibrium position Δq_i, respectively.[23]

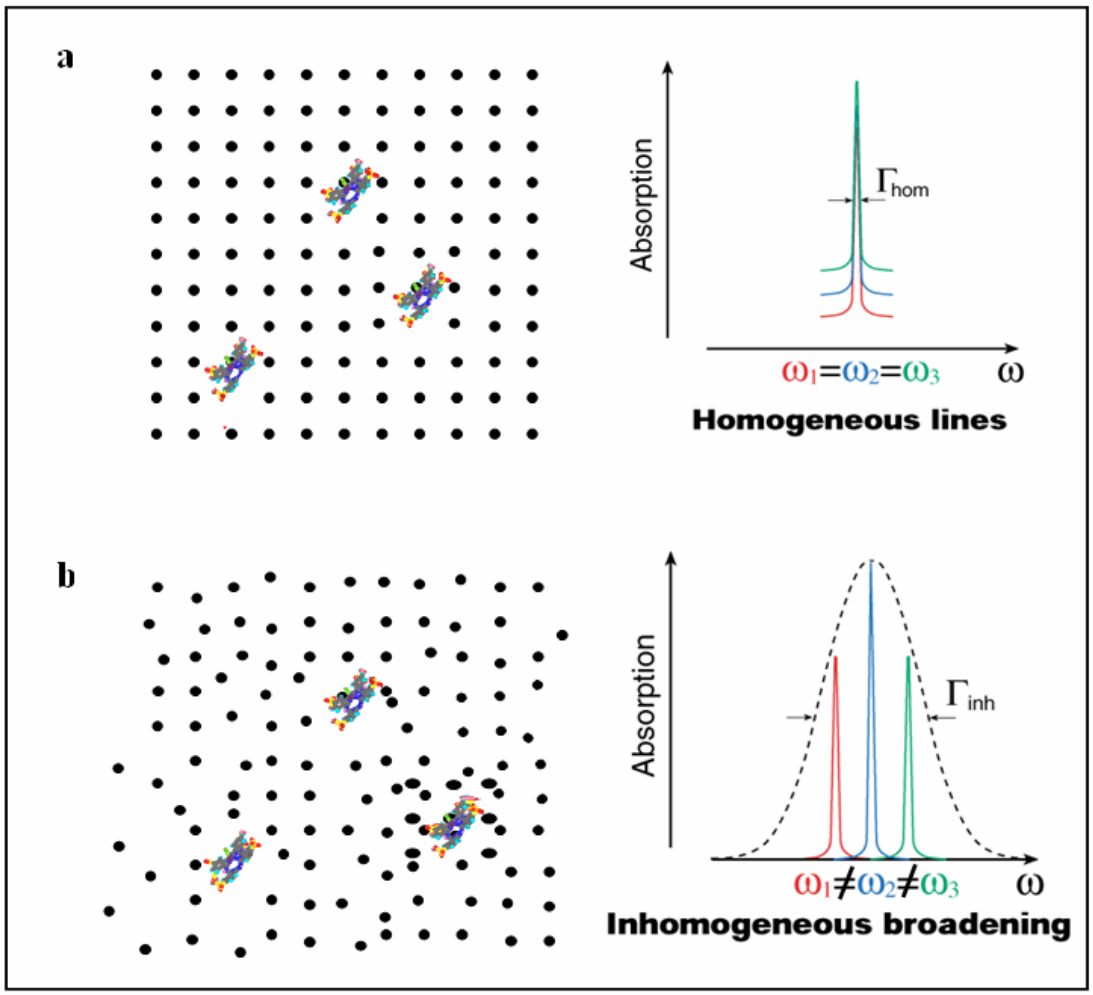

Figure I.2. Line broadening of impurity molecules in **(a)** perfect lattices and **(b)** imperfect lattices. **(a)** Homogeneous lines overlap in the absorption spectrum with a linewidth Γ_{hom}. **(b)** Each impurity molecule absorbs at a different frequency, which leads to an inhomogeneously broadened band with a width of Γ_{inh}.

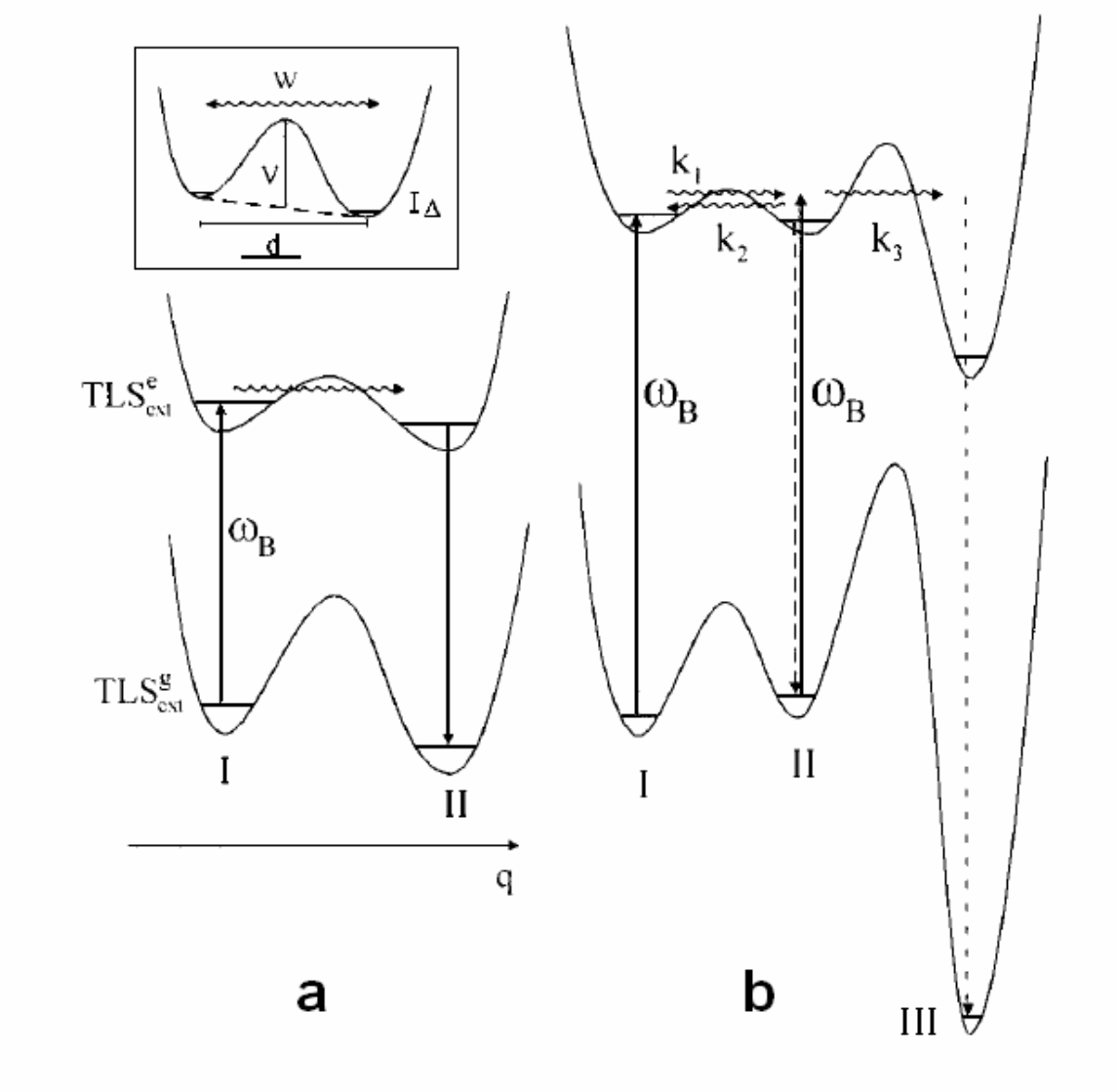

Figure I.3. Extrinsic TLS model **(a)** and MLS model **(b)** for NPHB. ω_B is the burn frequency of the laser and k_1, k_2, and k_3 are the tunneling rates. I, II, and III denote chromophore-host configurations where I corresponds to the pre-burn configuration and II and III correspond to post-burn configurations. W is the tunneling frequency, V is barrier height and Δ is the asymmetry of a TLS.[10] Note that while TLS can be a good approximation for low fluence hole burning, an MLS approximation becomes necessary at high fluences.[10]

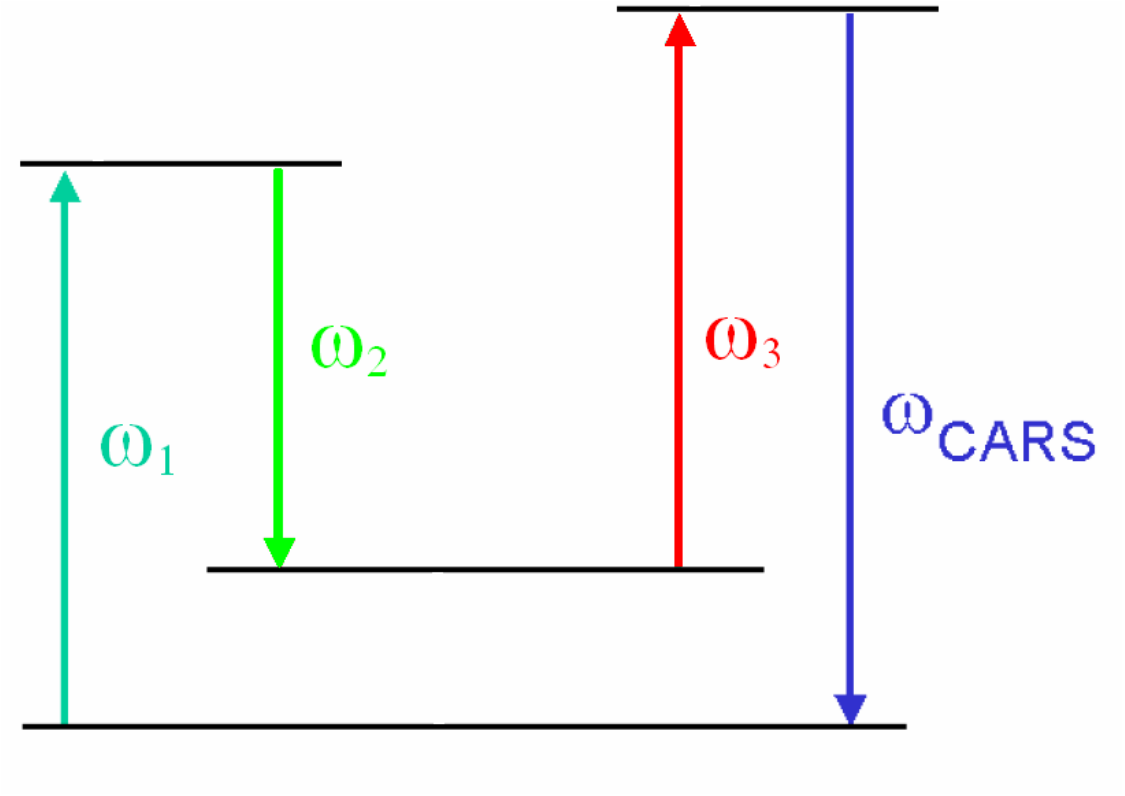

Figure II.1. CARS energy scheme. ω_1, ω_2, and ω_3 are usually called ω_{pump}, ω_{stokes} (or ω_{dump}), and ω_{probe}. The energy difference between ω_1 and ω_2 corresponds to the energy to excite Raman-active vibrational and/or rotational modes of molecules. The scheme shows energy conservation during the scattering process.

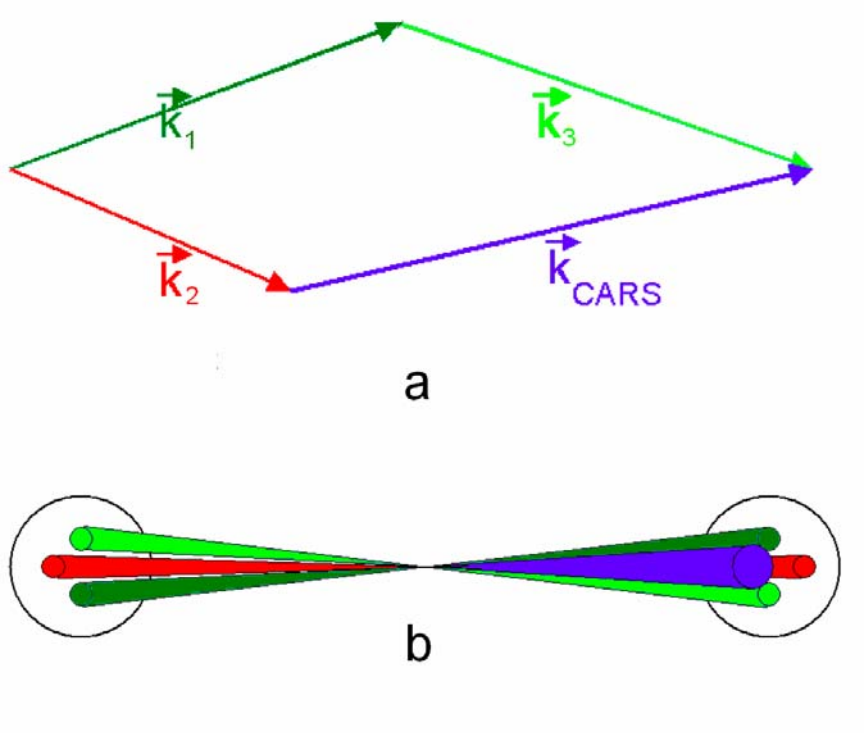

Figure II.2. Phase-matching of wave vectors in CARS. **(a)** Three-dimensional vector diagram of the phase-matching condition necessary to obtain maximum conversion efficiency in the four-color technique. **(b)** Spatial pattern of beams in folded BoxCARS geometry.

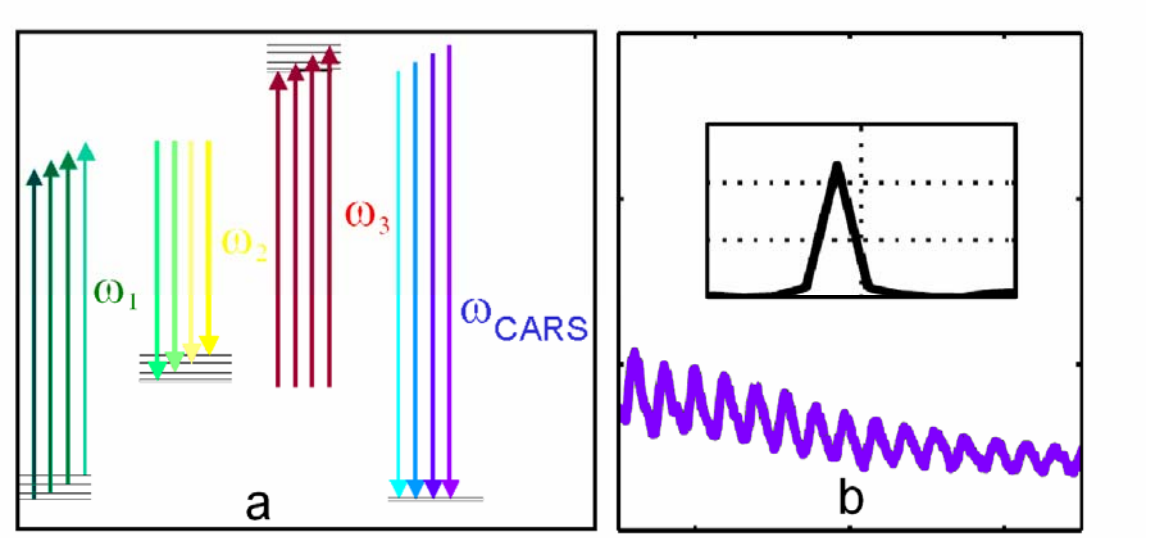

Figure II.3. (a) Broadband femtosecond laser pulses and **(b)** detected CARS signal (along with its Fourier-transformed frequency). Only one beat frequency is shown in part **(b)** for clarity. More than one beat frequency is possible.

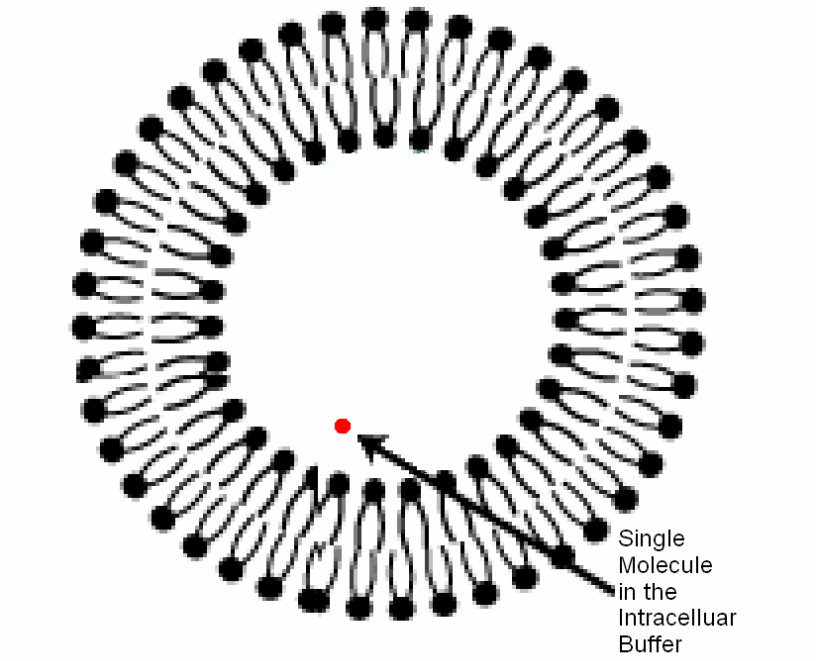

Figure III.1. Schematic presentation of the lipid bilayer of a liposome. Both intracellular and extracellular solutions are aqueous. The hydrophilic "heads" and the hydrophobic "tails" are well aligned to minimize the potential energy. Therefore, the lipid bilayer creates a boundary to encapsulate various particles and isolates them from the external surroundings.

CHAPTER 2. RED ANTENNA STATES OF PS I OF CYANOBACTERIA: STARK EFFECT AND INTERSTASTE ENERGY TRANSFER

A paper published in Journal of Physical Chemistry*

T.-M. Hsin, V. Zazubovich, J. M. Hayes, and G. J. Small

Abstract

Previously, Stark hole burning spectroscopy and effects of pressure at low temperature were used to determine the number of the red antenna states of the cyanobacteria *Synechococcus elongatus* and *Synechocystis PCC6803* (Hayes, J. M.; Matsuzaki, S.; Rätsep, M., Small, G. J. *J. Phys. Chem. B* **2000** *104,* 5625. Zazubovich, V.; Matsuzaki, S.; Rätsep, M.; Hayes, J. M.; Small, G, J. *Chem Phys.* **2002**, *275*, 47). Distinct differences in linear pressure shift rates, the magnitude of the permanent dipole moment change, $f\Delta\mu$, and electron-phonon coupling strength clearly show that in *Synechococcus,* there are three red states (C708, C715, and C719), while in *Synechocystis*, there are two red states (C708 and C714). In the Stark hole burning spectra of the lowest states of these two systems, hole splitting was not observed, only

---

* Reprint with permission from Journal of Physical Chemistry B **2004,** 108(29), 10515-10521.

hole broadening, for excitation polarization both parallel and perpendicular to the Stark field direction. The theories of Stark hole burning predict that splitting should occur for one of the polarizations, unless there is a large, random component to the induced dipole moment change, $\Delta\mu_{ind}$, which is not expected to be the case for pigment–protein complexes in which the orientations of pigments relative to the protein matrix are non-random. In this paper, Stark hole burning at higher resolution is used to re-investigate the absence of splitting. Even at higher resolution, however, no splitting is detected. This is explained by invoking large variations of the inherent dipole moment change $\Delta\mu_0$ of the dimer (the origin of the red state absorption), rather than of the induced dipole moment change. These arise from a distribution of the relative orientations and separations between the components of the dimer. This distribution also results in a random component of the polarizability change tensor, $\Delta\alpha$. The random components of $\Delta\mu_0$ and $\Delta\alpha$ not only obscure the Stark splitting, but also cause the large inhomogeneous broadening observed for these lowest energy red states. Temperature dependent hole widths were also measured for C708 and C714 of *Synechocystis*. For C714, a $T^{1.3}$ temperature dependence was observed, consistent with dephasing by the disordered protein matrix. At 708 nm, however, much higher fluences were required to saturate the absorption of the blue edge of the C714 band, and then begin to burn C708. The contribution of the C708 component to the broadening was weakly temperature dependent over the range measured, 2 to 14 K. This contribution is due to energy transfer from C708 to C714, and the width measured corresponds to an energy transfer time of 6 ps. This observation provides further proof for the existence of two red antenna states, C708 and C714.

1. Introduction

Elimination of the effects of static inhomogeneous broadening by spectral hole burning at low temperatures[1] has proven to be an invaluable technique for the study of complex molecular systems such as protein-pigment complexes. When such complexes contain significant protein-pigment and/or pigment-pigment interactions, the power of the spectral hole burning technique can be further enhanced by including the effects of external fields on the hole spectra. In particular, studies of photosynthetic pigment-protein complexes where excitonic coupling of the chlorophyll pigments and strong electron-phonon (pigment-protein) coupling are important for electron transfer and energy transfer have benefited greatly from including the effects of pressure[3-6] and electric fields (the Stark effect).[3,4,7,8]

For coupled pigments, the rate of linear pressure shifts to the red of spectral holes can be correlated with the coupling strength. In the case of weak coupling, linear shift rates $\leq |0.15\ \mathrm{cm^{-1}\,MPa^{-1}}|$ are typical. (Shift rates of –0.05 to –0.15 $\mathrm{cm^{-1}\,MPa^{-1}}$ are typical for the $\pi\pi^*$ transitions of isolated chromophores in polymers and glasses.[9,10]) On the other hand for strongly coupled pigments, linear shift rates of $\geq |0.3\ \mathrm{cm^{-1}\,MPa^{-1}}|$ are found. Such large shift rates have been argued to indicate that electron-exchange contributes significantly to the coupling.

In the case of strongly coupled pigments, the electronic transition is often associated with a large change in the permanent dipole moment of the molecule, which can arise, for example, when the excited state possesses significant charge transfer character. The magnitude of the change in dipole moment, $\Delta\mu$, can be measured by Stark spectroscopy. (Here and below, bold variables are vectors, regular variables are their

magnitudes.) For example, the bacteriochlorophyll *a* special pair (P870) of *Rhodobacter sphaeroides* reaction center has $f\Delta\mu = 5.2$ D,[11] where f is the local field correction factor. (Although a value of $f \approx 1.5$ is sometimes used, we prefer to report values as $f\Delta\mu$ since the dielectric constant of the protein medium is not known.) The large value of $f\Delta\mu$ for P870 can be contrasted with the values typical of monomeric chlorophyll *a* (Chl *a*), 0.5-0.6 D.[3,8]

The above points regarding pressure and Stark effects on hole spectra of Chl *a* in pigment-protein complexes are well illustrated in several papers on the red antenna states of PS I of cyanobacteria.[3,4] These states, absorbing light at energies lower than that of the primary electron donor, P700, have attracted considerable interest and remain incompletely understood.[12] Although these states can undergo upward energy transfer to P700 at physiological temperatures, it is not known if this is their primary function or if, e.g., photo-protection is more important.[13]

Interest in the red antenna states was further stimulated by the publication of the 2.5-Å-resolution crystal structure of PS I from *Synechococcus elongatus.*[14] In the structure, three dimers and a trimer of Chl *a* with Mg···Mg separations of ~8 Å were identified. It was speculated that some of these might be the source of the red absorbing states and papers proposing possible assignments of particular multimers to individual red absorptions have appeared.[15-17]

Pressure and electric field effects on the hole spectra of both *Synechococcus elongatus* and *Synechocystis PCC6803* were used by Small and co-workers to resolve the red state absorptions better.[3,4] In *Synechocystis*, where the red absorption consists of a single broad band at 708 nm even at 4 K, zero-phonon holes (ZPH) burned to the red side

of the band show much stronger electron-phonon coupling than holes burned on the high energy side, suggesting that there are (at least) two states underlying the absorption. This conclusion was reinforced by both Stark and pressure effects on the ZPHs, which had larger values of $f\Delta\mu$ (2.3 D at 714 nm) and of the linear pressure shifts (–0.45 cm^{-1} MPa^{-1} at 713 nm) than on the blue side of the band ($f\Delta\mu$ = 1.0 D at 708 nm, pressure shift rate is –0.17 cm^{-1} MPa^{-1} at 706 nm). From these results and from fitting the hole spectra as a function of the burn wavelength, λ_B, it was concluded that there are two red absorbing states at 714 nm (C714) and 708 nm (C708). Although these states exhibit considerable spectral overlap, C714 was definitely associated with a strongly coupled Chl *a* dimer, possessing significant charge transfer character.

Similar analysis and results were also obtained for *Synechococcus* where there are two red absorption bands (C708 and C719) resolvable in the low temperature absorption spectrum.[4,18] From the combination of hole burning with Stark fields and high pressure, an additional absorption or state (C715) was identified.[4] The lowest state C719 has properties very similar to those of C714 of *Synechocystis*, while the other two states have smaller values for $f\Delta\mu$ and linear shift rate but still larger than typically measured for monomeric antenna Chl *a*.

A puzzling feature of the Stark hole spectra of the cyanobacteria is the absence of splitting of the ZPH burned into the lowest-energy (red) antenna band.[3,4] In an electric field, the transition frequency of the molecule shifts as

$$\Delta\omega = \hbar^{-1}(f\boldsymbol{\Delta\mu}\cdot\boldsymbol{E}_S + \tfrac{1}{2}f^2\boldsymbol{E}_S\cdot\boldsymbol{\Delta\alpha}\cdot\boldsymbol{E}_S) \qquad (1)$$

where $\boldsymbol{\Delta\mu}$ is the permanent dipole moment change between excited and ground electronic states, $\boldsymbol{E}_S$ is the Stark field, $\boldsymbol{\Delta\alpha}$ is the polarizability difference tensor, and f is the local

field correction factor, as mentioned above. The first term in Eq. 1 describes the linear Stark effect while the second term is the quadratic Stark effect. In what follows, only the linear term will be of interest (i.e., it is relevant for the field strengths $\boldsymbol{E}_S$ used in the experiments). The dipole moment difference, $\Delta\boldsymbol{\mu}$, can be described as a sum of the free molecule dipole moment difference, $\Delta\boldsymbol{\mu}_0$, and the dipole moment difference induced by the protein lattice, $\Delta\boldsymbol{\mu}_{ind}$. According to refs 19-21, when $\Delta\boldsymbol{\mu}_0$ is dominant over $\Delta\boldsymbol{\mu}_{ind}$, a splitting of the ZPH should be observed for one of the two orthogonal polarizations of the exciting laser relative to the Stark field. However, if $\Delta\boldsymbol{\mu}_{ind}$ is dominant, and has a large random component, such as in a polymer or glass matrix, only hole broadening will be observed independent of laser polarization. It is in the view of this that the absence of the aforementioned splitting for the 714 nm and 719 nm states of *Synechocystis* and *Synechococcus* is surprising since the large $f\Delta\mu$ values of ~2.4 D are most reasonably attributed mainly to $f\Delta\boldsymbol{\mu}_0$ (of the dimer), not $f\Delta\boldsymbol{\mu}_{ind}$.

In this paper, the previous Stark results for PS I are reviewed and new non-photochemical hole burning (NPHB) results obtained at higher resolution (50 MHz) are reported. The intent of the higher resolution experiments is to determine if there is truly no ZPH splitting for the red-most antenna state of the cyanobacterial PS I or if the splitting was not observed due to limitations of the previous experiments. These limitations are not only due to moderate (~0.5-1 cm^{-1}) resolution per se. (The resolution in ref. 3 and 4 was determined by the resolution of the Fourier transform spectrometer. The laser bandwidth was ~2 GHz.) Note that the ZPH splitting can be observed when the polarized laser light creates anisotropy in the sample by burning only molecules (or states) with transition dipole moment approximately parallel to the laser light

polarization. The latter condition was quite likely not satisfied in the experiments of Rätsep et al.[3] and Zazubovich et al.,[4] since the holes used for the Stark effect measurements were close to saturated and/or fluence-broadened (in order to see holes of reasonable fractional depth despite the low resolution), and, as a result, the polarization selection of the transition dipole moments of the burned states could be lost. Since electron-phonon coupling for the C714 state is strong (Huang-Rhys factor $S \approx 2$ due to 18 and 70 cm^{-1} phonons), the maximal fractional ZPH depth, which can be achieved for this state is 0.13 (exp(-S)). Thus, 10%-deep holes may be already saturated enough to prevent observation of the splitting. In the experiments by Rätsep at al.[3] and Zazubovich et al.[4] the noise level was ~1 % of the signal, which resulted in hole depth-to-noise ratio of not more than 10 for 10 % deep (and probably saturated) holes at zero applied field. Broadening of the hole in the electric field resulted in further reduction of hole to noise ratio, making those holes barely detectable.

A second objective of this work is to find out if excitation energy transfer occurs from higher-energy red states to lower-energy ones and to determine the rate of such a transfer. Formation of a lower-energy (714 nm) satellite hole upon higher-energy (706 nm) excitation was observed for *Synechocystis*.[3] However, it was not clarified if this effect is due to energy transfer or due to structural changes, which accompany non-photochemical hole burning of the states directly excited. The shape of the non-line-narrowed emission spectrum (peaked at 722 nm) suggests that the C708 state does not fluoresce. Thus, experimental observations indicate that C708-C714 energy transfer most likely does occur. The issue will be clarified by precise determination of the

homogeneous widths of the ZPH burned into the C708 state; these widths are inversely proportional to the energy transfer time.

2. Experimental Section

The research was focused mainly on Photosystem I of *Synechocystis*. Since it has only two red antenna states, the results can be interpreted more easily. As we will see, the results for *Synechococcus* (less detailed studies performed) were similar. *Synechocystis* and *Synechococcus* wild type trimer PS I samples were prepared as described in refs 3 and 4 respectively. To improve the resolution, holes were probed in the fluorescence excitation mode as opposed to the absorption detection used in refs 3 and 4. Hole burning was carried out and the spectra were scanned using the Coherent 699-29 (Autoscan) laser at 50-MHz resolution. Laser intensity was stabilized with a CRI power stabilizer and attenuated with neutral density filters. The intensity when scanning was of the order of 2 $\mu W\ cm^{-2}$, the intensities used for burning were about 100 times higher. The total burning doses were in the range 0.001 to 0.27 $J\ cm^{-2}$, depending on the burn wavelength (i.e. at least 100 times smaller than those used in refs 3 and 4). Hole spectra were scanned within a 50-GHz window precisely centered at the burn wavelength. Fluorescence was detected at a 90^{o} angle (in relation to excitation) by a cooled photomultiplier (Hamamatsu) through an AELP730 interference filter (Omega optical). The Stark hole burning apparatus is described elsewhere.[8] Briefly, the sample in a gelatin capsule (Torpak) was squeezed between the electrodes of the Stark cell (distance between electrodes 4 mm). Voltages of up to 3.5 kV were obtained from a Trek model 610C high voltage power supply, which resulted in electric field strengths of up to

8750 V cm^{-1}. Experiments were performed for laser polarization both parallel and perpendicular to the Stark field. A polarization plane rotator (Thorlabs) was used to rotate the laser polarization by 90^{o}. The Stark cell was immersed into liquid helium in a Janis 8 DT cryostat with temperature controlled and stabilized at 2 K by a Lakeshore Cryotronic model 330 temperature controller.

To burn deep holes into the C708 band, it was necessary to use higher fluences. These holes were measured with a resolution of 6 GHz using no etalons in the burn laser (laser bandwidth 2 GHz). Holes were burned for several fluences (up to 100 J cm^{-2}) and holewidths extrapolated to zero fluence.

Some spectra exhibited a sinusoidal modulation. In order to account for that, the pre-burn spectrum was fitted to a sinusoid and that sinusoid was subtracted from the hole spectra before fitting to a Lorentzian shape. Alternatively, if the signal-to-noise ratio allowed, pre-burn spectra were subtracted from post-burn spectra before fitting.

3. Results

Figure 1 shows an example of a 6 % deep hole at 716 nm in PS I of *Synechocystis* in zero-field and the same hole in an applied field of 5.0 kV cm^{-1} with $\boldsymbol{E}_S \parallel \boldsymbol{E}_{laser}$. No splitting was observed in either polarization even for very shallow holes (3 % deep) which were used to insure that any splitting was not obscured by saturation of the hole. To determine $f\Delta\mu$, ~6 % deep holes were used, as a more reliable value could be obtained because of the higher signal-to-noise ratio of the deeper holes. Values for $f\Delta\mu$ were determined for several wavelengths in both parallel and perpendicular polarizations

(relative to the Stark field direction) using the theory of Kador et al.[22] The results are given in Table 1, and a representative plot of the hole width, Γ_{hole}, versus applied field is shown in Figure 2. For *Synechococcus*, measurements were made at 710 and 723 nm using parallel polarizations only. Values of $f\Delta\mu$ were similar to those for *Synechocystis* (i.e., 2.6 D and 1.6 D at 723 nm and 710 nm, respectively).

Table 1 also includes the values of $f\Delta\mu$ reported in ref 3. In that work, it was reported that within experimental error, there was no difference in the values measured for the two orthogonal polarizations. Although this might be true for λ_B = 707.5 nm in the present work, at longer wavelengths the effect for parallel polarization is significantly larger than for perpendicular. Also, note that in the earlier work, the dipole moment change clearly decreased below 708 nm (to ≤ 1 D), while in the present work, the values are nearly constant over the range of the experiment.

Turning to the hole widths, there is a weak wavelength dependence and a fluence dependence over the range from 716 nm to 707.5 nm. For example, at 716 nm the width was 2-3 GHz for a 3 % deep hole, increasing to 6-7 GHz for a 10 % deep hole. At 709 nm, on the other hand, the width was 4-5 GHz at the lowest fluence used, with a depth of 3 %. Increasing the fluence to that used to burn the 10 % deep hole at 716 nm caused a slight increase in depth to 4 % while increasing the width to 8-9 GHz. Further increases in fluence did not increase the hole depth but rather caused broadening. Our inability to burn deep narrow holes at ~708 nm, as well as the results of Stark experiments (see above), indicate consistently that shallow holes burned in this wavelength range belong to the higher-energy side of the broad C714 band. This is the reason that the $f\Delta\mu$ values obtained at ~708 nm differ from those reported in ref 3. Because of the much higher burn

fluence used in ref 3, the C708 state was preferentially probed in that work for burn wavelength around 708 nm. A small contribution from the C714 state to spectral hole burned in that region was not resolved in ref 3. In the present work, the slight decrease in $f\Delta\mu$ values with the decrease of the burn wavelength may be explained by the C708 state just starting to contribute to the spectral holes for the burn fluences used. The significant (at least an order of magnitude) difference in hole burning efficiencies for the C714 and C708 states is most easily explainable assuming different excited state lifetimes. That the $f\Delta\mu$ value for 15-GHz (in zero-field) 4%-deep ZPH was still close to 2 D, indicates that the lifetime of the C708 state is shorter than 20 ps. Because a reliable determination of the ZPH widths larger than 15 GHz in high-resolution mode is somewhat problematic, we switched to lower-resolution (6 GHz) mode to determine the lifetime of the C708 state precisely. Using a broader burn laser (2 GHz), and fluences such as used in refs 3 and 4 (up to 100 J cm^{-2}), a 10%-deep hole with a width of 1.7 cm^{-1} was obtained at 707 nm. (The widths given so far were all obtained at 2 K.) The broad holes burned in the C708 band exhibited a slow increase of the homogeneous ZPH width with temperature. This indicates that the ZPH width is, in case of the C708 band, determined mainly by a temperature-independent process (most likely energy transfer, see Discussion), with some contribution from dephasing. An example of a 2.0 cm^{-1} wide hole burned at 708.4 nm at 10 K is shown in Figure 3. For the C714 band (λ_B = 715-716 nm), the ZPHs broadened according to a $T^{1.3}$ power law over the range from 2 to 14 K (results not shown). Thus, the width of the ZPHs burned into C714 band is determined by TLS-assisted dephasing only.

4. Discussion

A: Stark Hole Burning Results. Under high resolution and optimum conditions Stark splitting of the ZPH burned into the red-most C714 and C719 absorption bands of *Synechocystis* and *Synechococcus* was not observed. The only photosynthetic pigment-protein complex in which a splitting has been observed in the Stark hole burning spectrum is the Fenna-Matthews-Olsen (FMO) protein.[8] FMO is a trimeric antenna complex from green sulfur bacteria. Each of the three proteins, which make up the intact complex contain seven bacteriochlorophyll *a* molecules. Coupling between BChl *a* belonging to different proteins is weak and the lowest energy absorption band (825 nm) of the complex is due to a single BChl *a* in each protein. Because coupling between these three BChl *a* is weak, the 825 nm band is the sum of three transitions which would be degenerate except for structural disorder. The properties of this state are nearly ideal for the observation of splitting in the Stark hole spectra from the viewpoint of the relevant theories,[19-21] according to which hole splitting is best resolved when the angle, γ, between the transition dipole moment, $\boldsymbol{D}$, and $\boldsymbol{\Delta\mu}$ is ~ 0° and the laser polarization, $\boldsymbol{E}_L$, is parallel to $\boldsymbol{E}_S$, the Stark field. Such was the case for the FMO complex. In ref 8, it was estimated that $\gamma < 15°$. Furthermore, the Stark broadening which occurs along with splitting was small, so that the splitting was more easily resolved. Also, as is often the case when excitonic coupling is weak, the electron-phonon coupling is also weak for the FMO system, so that a ZPH could be burned with high signal-to-noise ratio. Finally, inhomogeneous broadening is relatively small in FMO (~70 cm^{-1}), which correlates with smaller contributions from the random components of $\boldsymbol{\Delta\mu}$, (*vide infra).*

Turning to the lack of ZPH splitting in this work for the red-most antenna states of *Synechocystis* and *Synechococcus*, let us consider first the source of the hole broadening induced by the Stark field. The only broadening mechanism included in the theories in their simplest form (see Fig 6 by Kohler et al. or Fig 2 by Schatz and Meier) is broadening due to $cos^2\upsilon$ (where υ is the angle between the transition dipole $\boldsymbol{D}$ and the laser polarization $\boldsymbol{E}_L$) *i.e.* the spatial distribution of the transition dipoles of the burned molecules. This broadening is always present, even if $\Delta\mu_{ind} = 0$. According to this simplified theory, splitting should be observed for one laser polarization or the other, although it should be less resolvable for $\gamma \approx 90^o$ than for $\gamma \approx 0^o$. Following Schätz and Maier[20] (a less detailed discussion, without the calculation of sample hole spectra, is given also in refs 19 and 21), we write the matrix-induced term as

$$\Delta\mu_{ind} = \Delta\boldsymbol{\alpha}\cdot\boldsymbol{E}_{\text{int}} \tag{2}$$

where $\boldsymbol{E}_{\text{int}}$ is the field induced at the position of the chromophore by the surrounding lattice. $\Delta\mu_{ind}$ can be represented as a sum of fixed (in the frame of chromophore molecule) and random contributions:

$$\Delta\boldsymbol{\mu}_{\text{ind}} = \Delta\boldsymbol{\mu}_{\text{ind,fixed}} + \Delta\boldsymbol{\mu}_{\text{ind,random}} \tag{3}$$

The angle for γ between $\boldsymbol{D}$ and $\Delta\boldsymbol{\mu}_0$ is considered well defined. It is obvious from Eqs. 1-3 that if $\Delta\boldsymbol{\mu}_{\text{ind,random}}$ is dominant over $\Delta\boldsymbol{\mu}_{\text{fixed}} = \Delta\boldsymbol{\mu}_{\text{ind,fixed}} + \Delta\boldsymbol{\mu}_0$ then no hole splitting is expected for any polarization, only broadening. (This is the case treated by Kador et al. [22], for small variance in the magnitude of the randomly oriented dipole moment change.) A less obvious result follows from the detailed simulations by Schätz and Maier:[20] lack of splitting can also occur even if $\Delta\boldsymbol{\mu}_{\text{ind,random}}$ is not dominant. For example, for $\boldsymbol{D}$ and $\Delta\mu_{\text{fixed}}$ approximately perpendicular, splitting is not observable already for $|\Delta\mu_{\text{fixed}}|$

$/|\Delta\mu_{ind,random}| = 2$ (see fig. 8C in ref 20). As was mentioned above, in photosynthetic complexes the orientation of chlorophylls in relation to the protein is approximately fixed and $\Delta\mu_{ind,random}$ is not expected to be large. However, because of structural disorder, it is not expected to be zero either. (The rough analysis given below indicates that random and fixed contributions may be of comparable magnitude for C714 of *Synechocystis*, even if the results are interpreted so as to maximize $\Delta\mu_{fixed}$.) Significant static inhomogeneous broadening (~50-200 cm^{-1}) of Chl $S_1(Q_y) \leftarrow S_0$ absorption bands is generally observed in photosynthetic complexes. This broadening may be treated in terms of the solvent shift and expressed through the same variables as used above:[19]

$$\Delta\omega_{solvent\ shift} = -\hbar^{-1}(\Delta\boldsymbol{\mu}_0\boldsymbol{E}_{int} + 1/2\ \boldsymbol{E}_{int}\cdot\Delta\boldsymbol{\alpha}\cdot\boldsymbol{E}_{int}) \qquad (4)$$

The solvent shift depends only on the parameters of the chromophore ($\Delta\boldsymbol{\mu}_0$ and $\Delta\boldsymbol{\alpha}$) and the "pocket field" $\boldsymbol{E}_{int}$. It is not dependent on the external field. Based on Eq. 4, the inhomogeneous broadening is positively correlated with the degree of orientational and translational disorder and with the magnitude of the random contribution to $\boldsymbol{E}_{int}$, resulting in a large $\Delta\mu_{ind,random}$ value. We emphasize that the inhomogeneous broadening for the C714 state of PS I of *Synechococcus* is unusually large ~300 cm^{-1},[23] while the lowest energy band of the FMO complex consists of three quasi-degenerate bands each with a width of only ~70 cm^{-1}.

Next, taking into account that C714 is the lowest exciton component of a dimer, the frequency of the electronic transition for the C714 state is determined not only by diagonal disorder (described in the previous paragraph as differences in solvent shifts) but also off-diagonal disorder, which is due to differences in the inter-pigment couplings from complex to complex. These differences result from the variations in distance and

mutual orientation of the chlorophylls of the dimer. The distribution of orientations of the pigments in relation to each other results in the distribution of the angle γ between $\boldsymbol{D}$ and $\Delta\boldsymbol{\mu}_0$ as well as distributions of the magnitudes of both vectors. (Here $\boldsymbol{D}$ and $\Delta\boldsymbol{\mu}_0$ are redefined as the transition dipole moment of the lowest state and permanent dipole moment change, respectively, for a "free" dimer.) In other words, in the case of a dimer in a glass-like protein both $\Delta\boldsymbol{\mu}_0$ and $\Delta\boldsymbol{\mu}_{\text{ind}}$ have a random component.

$$\Delta\boldsymbol{\mu}_0 = \Delta\boldsymbol{\mu}_{0,\text{fixed}} + \Delta\boldsymbol{\mu}_{0,\text{random}} \tag{5}$$

It is quite likely that the components of the polarizability difference tensor $\Delta\boldsymbol{\alpha}$ for the lowest state of the dimer are also subject to a distribution, for the same reasons that there is a distribution of $\Delta\boldsymbol{\mu}_0$. We stress that whereas for a monomeric chromophore the origin for a distribution of $\Delta\boldsymbol{\mu}_{\text{ind}}$ is a distribution of $\boldsymbol{E}_{\text{int}}$ only, for the dimer there are distributions of both $\boldsymbol{E}_{\text{int}}$ and $\Delta\boldsymbol{\alpha}$.

The quantity observable in Stark hole burning experiments is the magnitude of

$$\Delta\boldsymbol{\mu}_0 = \Delta\boldsymbol{\mu}_{0,\text{fixed}} + \Delta\boldsymbol{\mu}_{0,\text{random}} + \Delta\boldsymbol{\mu}_{\text{induced,fixed}} + \Delta\boldsymbol{\mu}_{\text{induced,random}} \tag{6}$$

The right side of Eq. 6 is a vector sum, so fixed and random contributions can be grouped together. If the fixed components fully cancelled each other, splitting would be unobservable for any angle γ and the values of $f\Delta\mu$ would be equal for both polarizations. Although hole splitting is not resolved in our experiments, the observations indirectly suggest that splitting may be present, but hidden by the broadening. First, the difference in $f\Delta\mu$ values for different polarizations observed here, but not in ref 3 or 4, may be due to splitting for parallel polarization. It has also been observed that the $f\Delta\mu$ values obtained from the shallowest holes (less reliable) are systematically larger than those obtained from more saturated holes. For example, values of 2.9 and 2.2 D were obtained

for parallel and perpendicular polarizations, respectively, for a 3 % deep hole burned at 716 nm. If these values are correct, they may indicate the presence of a fixed contribution to $f\Delta\mu$ that gradually becomes unobservable with the loss of the ensemble anisotropy by hole saturation. In order to be more specific, we present an alternative analysis of the hole spectra from Figure 1. The bottom of the 5 kV cm^{-1} hole shown is slightly flattened, which may indicate the onset of hole splitting. Although a good fit is obtained by fitting this hole to a single Lorentzian, a similarly good fit can also be obtained by using two 10-GHZ-wide Lorentzians, separated by 6 GHz. From such a shape, a rough estimate of $f\Delta\mu_{fixed}$ is 1.2 D for zero angle between $f\boldsymbol{\Delta\mu}_{fixed}$ and $\boldsymbol{D}$, based on $\Delta\omega_{split} = f\Delta\mu E_S \cos\varphi$, with φ being the angle between $\boldsymbol{\Delta\mu}$ and $\boldsymbol{E}_S$. If $\boldsymbol{E}_S \parallel \boldsymbol{E}_{laser} \parallel \boldsymbol{D}$, then $\cos\varphi \approx 1$, and an estimate for $f\Delta\mu_{random}$ is ~1.8 D, according to the theory of Kador et al.[22] This value agrees well with those measured for the perpendicular polarizations. Note, however, that because $\Delta\boldsymbol{\mu}_{random} = \Delta\boldsymbol{\mu}_{0,random} + \Delta\boldsymbol{\mu}_{induced,random}$ the condition of small variance in the magnitude of $\Delta\boldsymbol{\mu}_{random}$ may not be satisfied. There is also no reason to believe that the angle between $\Delta\boldsymbol{\mu}_{fixed}$ and the transition dipole moment $\boldsymbol{D}$ is indeed zero. A ~25° angle was initially estimated by Lockhart and Boxer using Stark modulation spectroscopy for the lowest state of the special pair of the bacterial RC.[24] This angle increased to ~38° and to ~45° with subsequent refinements of the analysis.[11,25]

To explain the "real" lack of splitting, one may assume, in addition to large fluctuations in $\Delta\boldsymbol{\mu}_0$, $\Delta\boldsymbol{\alpha}$ and $\boldsymbol{E}_{int}$, that the angle γ' (between $\boldsymbol{D}$ and $\Delta\boldsymbol{\mu}_{fixed}$) is closer to 90^0 than to 0^o. As mentioned above, in the latter case splitting is less pronounced even for $\Delta\boldsymbol{\mu}_{random} = 0$. However, $\gamma' \approx 90^o$ would be in contradiction with broadening of the hole being faster for parallel laser polarization and external field direction.

Some discussion on recent Stark modulation spectroscopy results by Frese et al.[26] is also in order. Frese et al. performed their experiments at 77 K in magic angle configuration, which eliminates any dependence on γ and on the precise shape of $\Delta\alpha$. They observed that $\mathrm{Tr}(\Delta\alpha) = 600$ Å$^3 f^{-2}$ for C719 of *Synechococcus* and $\mathrm{Tr}(\Delta\alpha) = 275$ Å$^3 f^{-2}$ for the red antenna band of *Synechocystis* (the two different states were not resolved). First, since Frese et al. did not resolve the C708 and C714 bands of *Synechocystis*, the value of 275 Å$^3 f^{-2}$ is most likely an average value for the two states and the value for C714 alone should be closer to 600 Å$^3 f^{-2}$ as measured for *Synechococcus*. Previous hole burning spectroscopy results have shown that properties of C714 of *Synechocystis* and C719 of *Synechococcus* are very similar.[3,4] The inability to resolve the C708 and C714 band is probably why a very small (compared to that of C719) dipole moment change ($f\Delta\mu = 0.4$ D) was observed for the red band of *Synechocystis*. We assume that the "correct" value for $f\Delta\mu$ for C714 obtained by modulation Stark spectroscopy would be close to that for C719 of *Synechococcus* (i.e. 3.6 D ± 15 %). Random components were not considered in ref 11 and 26. Note that for $f\Delta\mu_{\mathrm{fixed}} = 3.6$ D the hole splitting would be observed much better than it really is. Thus, it is another example of the $f\Delta\mu$ values obtained by modulation spectroscopy exceeding those obtained with hole burning. For a pocket field of the order of 10^6 V/cm the polarizability difference values reported by Frese et al. would yield ~2 D for $f\Delta\mu_{\mathrm{ind}}$.

A meaningful independent estimation of different components of $\Delta\mu$ requires detailed knowledge about the nature of the charge-transfer state, as well as about the structure of the protein pocket. This, in turn, requires assigning of C714 state to some chlorophyll aggregate known from structure data. Such data is not available for

Synechocystis. On the other hand, recent observations that the structure of plant PS I[27] is very similar to that of *Synechococcus* suggests that the latter structure could be used for *Synechocystis* without producing significant errors. One can argue that the dimer with the smallest Mg···Mg distance of 7.6 A (B37-B38)[14] is the most likely candidate for the origin of the charge transfer state. This dimer is the one for which high interpigment couplings were obtained in various approximations.[15,16] Site energies of individual chlorophylls, as estimated in ref 16, are also reasonably low. Although this dimer was rejected[15,16] as being a red state based on its lower excitonic state being less intense than the higher state, we believe it is not necessarily a problem. Quite the opposite, it is in agreement with the total absorption strength of the red antenna states of *Synechocystis* being approximately equal to that of ~3 Chl *a* molecules and with the relative weakness of the C719 band in *Synechococcus* when the presence of the C715 state is taken into account. Recently, Gobets et al.[28] proposed that the C719 state of *Synechococcus* originates from the B31/32/33 trimer. However, such an interpretation ignores the fact that several properties of C719 of *Synechococcus* are essentially identical to those of the C714 of *Synechocystis*,[3,4] which does not contain a trimer. These properties are $f\Delta\mu$, the linear pressure shift rate, the electron-phonon coupling and static inhomogeneous broadening. Although agreement in assigning the red-most state to a particular dimer has definitely not been reached, it is widely accepted that the red antenna states are the lowest exciton states of strongly coupled chlorophylls.

B: Energy transfer between the red antenna states. Next, we consider the hole widths. The $T^{1.3}$ dependence of the ZPH width Γ_{ZPH} is commonly seen for the dephasing of chromophores in disordered solvents.[29,30]

$$\Gamma_{ZPH}(T) = \Gamma_{ZPH}(T=0) + a\, T^{1.3} \quad (7)$$

It is not surprising to see this dependence for the C714 state, as the holes are burned by a non-photochemical mechanism, which also depends upon the protein matrix being disordered. Similar behavior was observed for the lowest-energy states of several photosynthetic complexes. The values of the pre-factor *a* were 0.2 GHz/K$^{1.3}$ for FMO,[31] 0.2 GHz/K$^{1.3}$ for CP-43[7], 0.35 GHz/K$^{1.3}$ for PS-II-RC[32,33], as well as ~3 GHz/K$^{1.3}$ for B870 band of LH-2[34] and ~1 GHz/K$^{1.3}$ for LHC-II.[35] (The latter two values were, however, obtained with low spectral resolution.) a = 0.9 GHz/K$^{1.3}$ observed for the C714 band of the *Synechocystis* PS I lies within the same range.

Of more interest is the behavior of the holes near 708 nm. First, there are two possible explanations of why burning deep (ZPHs with the fractional depth of ~15 % and the width of ~2 cm^{-1} were burned at 706-708 nm by Rätsep et al.[3]) narrow holes at ~708 nm is impossible in fluorescence excitation mode. According to the first scenario, the C708 state does not transfer energy to C714 state. In this case, the C708 state must contribute much less to the fluorescence excitation spectrum than to the absorption spectrum. (Note that the electron-phonon coupling is smaller for C708 than for C714 state. In the absence of energy transfer, the emission from the C708 state would be peaked at ~710 nm and detected much less efficiently than that from the C714 state with our experimental setup including >730 nm cut-off filter.) Figure 4 represents the broad-range fluorescence excitation spectrum of *Synechocystis* PS I. It is obvious from Figure 4 that at wavelengths longer than ~695 nm the fluorescence excitation spectrum (dashed line) is a perfect match for the absorption spectrum (solid line). Thus, the C708 does contribute to the fluorescence excitation spectrum. (The discrepancies at shorter

wavelengths may be real and reflect the fact that part of the energy harvested by antenna pigments is not transferred to the C714 state. Alternatively, these discrepancies may be an experimental artifact due to too high optical density of the sample at these wavelengths causing reabsorption effects.) Note also, that the nonline-narrowed emission spectrum of PS I of *Synechocystis* is peaked at ~722 nm[3] and does not contain any noticeable shoulder at ~710 nm, where the emission from the C708 state would be expected. Finally, the observation that it is possible to burn ~10%-deep ZPHs, though broad, at 708 nm in fluorescence excitation mode also argues against the C708 state not contributing to the fluorescence excitation spectrum.

Consequently, we reject the above scenario and conclude that the C708 $\rightarrow$ C714 energy transfer does occur and that it is fast, which results in hole burning efficiency for the C708 state being orders of magnitude lower than for the C714 state. Thus the failure to burn deep holes at ~708 nm at low fluence is explained attributing the observed shallow narrow holes to the blue edge of the C714 band, rather than to the C708 band. According to ref 23, about 20 % of the absorption at 708 nm is due to C714, which is consistent with being able to burn only ~4 % ZPH, given the Huang-Rhys factor for the C714 state. For higher fluence and a 2-GHz laser bandwidth, the observed ~10 % holes, with widths of ~1.7 cm^{-1} at 2 K, are no doubt due to burning into the C708 band, followed by energy transfer to the C714 state. The hole width is determined by energy transfer time, ~6 ps. The presence of such an energy transfer is an additional proof of existence of two distinct red antenna states in *Synechocystis* PS I.

Acknowledgment

Research at the Ames Laboratory was supported by the Division of Chemical Sciences, Office of Basic Energy Sciences, U.S. Department of Energy. Ames Laboratory is operated for USDOE by Iowa State University under Contract W-7405-Eng-82. We are deeply thankful to Dr. Parag Chitnis for providing *Synechocystis* PS I samples and to Dr. Tonu Reinot and Nhan Dang for help in operating their experimental system.

References and Notes

1. *Persistent spectral Hole-Burning: Science and Applications*; Moerner, W. E. Ed.; Springer: Berlin, 1988.
2. Wu, H.-M.; Rätsep, M.; Jankowiak, R.; Cogdell, R. J.; Small, G. J., *J. Phys. Chem. B* **1997**, *101*, 7641.
3. Rätsep, M.; Johnson, T. W.; Chitnis, P. R.; Small, G. J., *J. Phys. Chem. B* **2000**, *104*, 836.
4. Zazubovich, V.; Matsuzaki, S.; Johnson, T. W.; Hayes, J. M.; Chitnis, P. R.; Small, *Chem. Phys.,* **2002**, *275*, 47.
5. Zazubovich, V.; Jankowiak, R.; Small, G. J., *J. Phys. Chem. B* **2002**, *106*, 6802.
6. Wu, H.-M.; Rätsep, M.; Jankowiak, R.; Cogdell, R. J.; Small, G. J., *J. Phys. Chem. B* **1998**, *102*, 4023.
7. Jankowiak, R.; Zazubovich, V.; Rätsep, M.; Matsuzaki, S.; Alfonso, M.; Picorel, R.; Seibert, M.; Small, G. J., *J. Phys. Chem. B* **2000**, *104*, 11805.
8. Rätsep, M.; Wu, H.-M.; Hayes, J. M.; Blankenship, R. E.; Cogdell, R. J.; Small, G. J.; *J. Phys. Chem. B* **1998**, *102*, 4035.

9. Pschierer, H.; Friedrich, J.; Falk, H.; Schmitzberger, W., *J. Phys. Chem*., **1993**, *97*, 6902.

10. Renge, I., *J. Phys. Chem*. *A* **2000**, *104*, 3869.

11. Middendorf, T. R.; Mazzola, L. T.; Lao, K.; Steffen, M. A.; Boxer, S. G., *Biochem. Biophys. Acta,* **1993**, *1143*, 223.

12. Gobets, B.; van Grondelle, R., *Biochem. Biophys. Acta*, **2001**, *1507*, 80.

13. Karapetyan, N. V.; Holzwarth, A. R.; Rögner, M., *FEBS Lett*. **1999**, *460*, 395.

14. Jordan, P.; Fromme, P.; Witt, H. T.; Klukas, O.; Saenger, W.; Krauβ, N., *Nature*, **2001**, *411*, 909.

15. Sener, M. K.; Lu, D.; Ritz, T.; Park, S.; Fromme, P.; Schulten, K., *J. Phys. Chem*. *B* **2002**, *106*, 7948.

16. Damjanovic, A.; Vaswani, H. M.; Fromme, P.; Fleming, G. R., *J. Phys. Chem*. *B* **2002**, *106*, 10251.

17. Byrdin, M.; Jordan, P.; Krauβ, N.; Fromme, P.; Stehlik, D.; Schlodder, E., *Biophys. J*., **2002**, *83*, 433.

18. Pälsson, L.-O.; Dekker, J. P.; Schlodder, E.; Monshouwer, R.; van Grondelle, R., *Photosyn. Res*. **1996**, *48*, 239.

19. Köhler, M.; Friedrich, J.; Fidy, J., *Biochem. Biophys. Acta*, **1998**, *1386*, 255.

20. Schätz, P.; Maier, M., *J. Chem. Phys*., **1987**, *87*, 809.

21. Meixner, A. J.; Renn, A.; Bucher, S. E.; Wild, U. P., *J. Phys. Chem.,* **1986**, *;*, 6777.

22. Kador, L.; Haarer, D.; Personov, R., *J. Chem. Phys*., **1987**, *86*, 5300.

23. Hayes, J. M.; Matsuzaki, S.; Rätsep, M., Small, G. J., *J. Phys. Chem*. *B* **2000**, *104*, 5625.

24. Lockhart, D. J.; Boxer, S. G., *Biochemistry*, **1987**, *26*, 664.

25. Lockhart, D. J.; Boxer, S. G., *Proc. Natl. Acad. Sci. USA*, **1988**, *85*, 107.

26. Frese, R. N.; Palacios, M. A.; Azzizi, A.; van Stokkum, I. H. M.; Kruip, J.; Rögner, M.; Karapetyan, N. V.; Schlodder, E.; van Grondelle, R.; Dekker, J. P., *Biochem. Biophys. Acta*, **2002**, *1554*, 180.

27. Ben-Shem, A.; Frolow, F., Nelson, N., *Nature*, **2003**, *426*, 630.

28. Gobets, B.; van Stokkum, I. H. M.; van Mourik, F.; Dekker, J. P.; van Grondelle, R., *Biophys. J.*, **2003**, *85*, 3883.

29. Narasimhan, L. P.; Littau, K. A.; Pack, D. W.; Bai, Y. S.; Elschner, A.; Fayer, M. D., *Chem. Rev.* **1990**, *90*, 439.

30. Reinot, T.; Kim, W.-H.; Hayes, J. M.; Small, G. J. *J. Chem. Phys.* **1996**, 104, 793.

31. Matsuzaki, S.; Zazubovich, V.; Rätsep, M.; Hayes, J. M.; Small, G. J., J. Phys. Chem. *B* **2000**, *104*, 9564.

32. Groot, M. L.; Dekker, J. P.; van Grondelle, R.; den Hartog, F. T. H.; Völker, S., *J. Phys. Chem.* **1996**, *100*, 11488.

33. den Hartog, F. T. H., Vacha, F., Lock, A. J., Barber, J., Dekker, J. P., Völker, S., *J. Phys. Chem. B* **1998**, *102*, 9174.

34. Wu, H.-M.; Ratsep, M.; Lee, I.-J.; Cogdell, R. J.; Small, G. J.; *J. Phys. Chem. B*, **1997**, *101,* 7654.

35. Pieper, J.; Ratsep, M.; Jankowiak, R.; Irrgang, K.-D.; Voigt, J.; Renger, G.; Small, G. J., *J. Phys. Chem. A.* **1999**, *103,* 2412.

Table 1. Changes in permanent dipole moment for the red antenna states.

	λ (nm)	$f\Delta\mu$ (D)		
		⊥ and ∥[a]	∥[b]	⊥[b]
Synechocystis	690	0.5		
	692	0.6		
	695	0.5		
	698.5	0.7		
	702	0.6		
	707.5	0.8	1.9	1.7
	708	1.0	2.5	
	709		2.4	1.9
	710	2.0		
	712	1.8	2.5	1.8
	714	2.3		
	716	2.4	2.6	2.0
Synechococcus	692	0.5		
	694	0.7		
	696	0.8		
	698	0.5		
	701	0.6		
	704	0.8		
	706	0.6		
	708	0.7		
	710	1.0	1.6	
	712	1.0		
	714	1.3		
	716	2.2		
	718	2.2		
	720	2.3		
	723		2.6	

[a] *Synechocystis* values are from ref 3; *Synechococcus* values are from ref 4.
[b] All values from this work. Error is ± 0.2 D

Figure Captions

Figure 1: Experimental hole spectra (solid lines) and Lorentzian fits (dashed lines) for λ_B=716 nm, laser polarization parallel to the direction of the Stark field and the field strengths of 0 and 5 kV cm^{-1}. Burn fluence was ~0.01 J cm^{-2}. For ZPH widths for intermediate field strengths see Figure 2. T=2K.

Figure 2: The dependence of the ZPH width on the external electric field for the ~6%-deep hole (see Figure 1) burned at 716 nm (♦) and the best fit based on the model [22] (solid line). Laser polarization was parallel to the direction of the Stark field and the burn fluence was ~0.01 J cm^{-2}. $f\Delta\mu$ = 2.7 D.

Figure 3: Experimental hole spectrum (—) and Lorentzian fit (---) for λ_B=708.4 nm. Burn fluence was ~100 J cm^{-2}; fractional ZPH depth is 7-8 %; T = 10K.

Figure 4: Absorption (—, from Ref 3) and fluorescence excitation (---, this work) spectra of the PS I from *Synechocystis*. T = 5K.

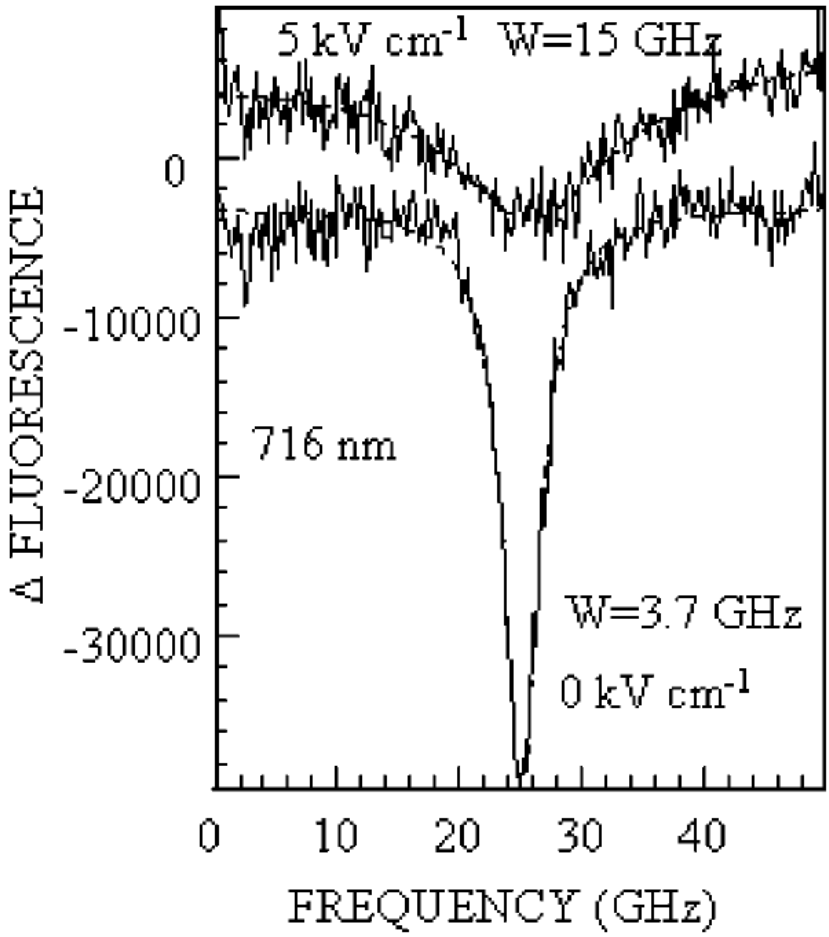

Figure 1.

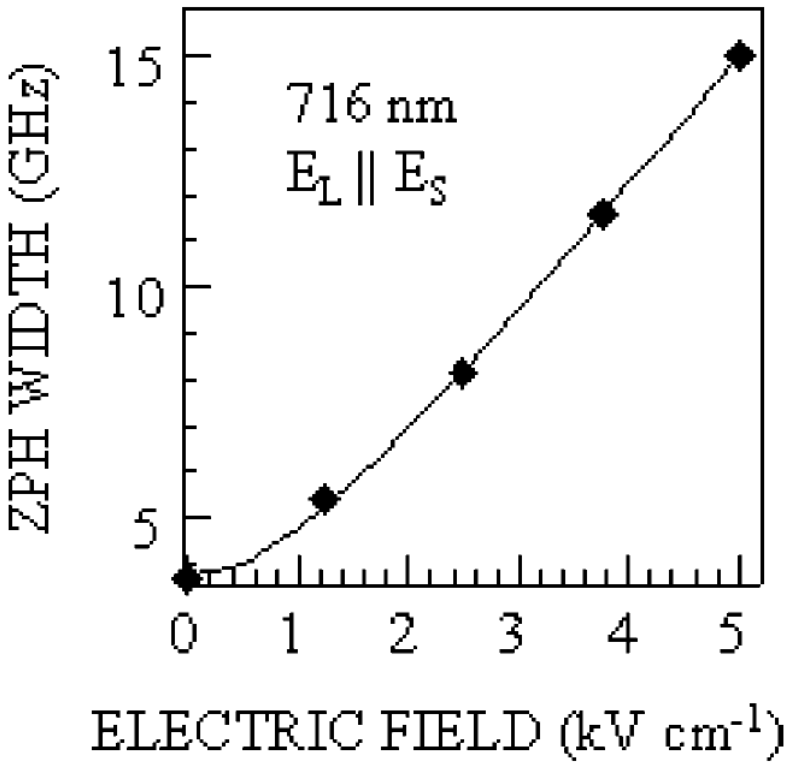

Figure 2.

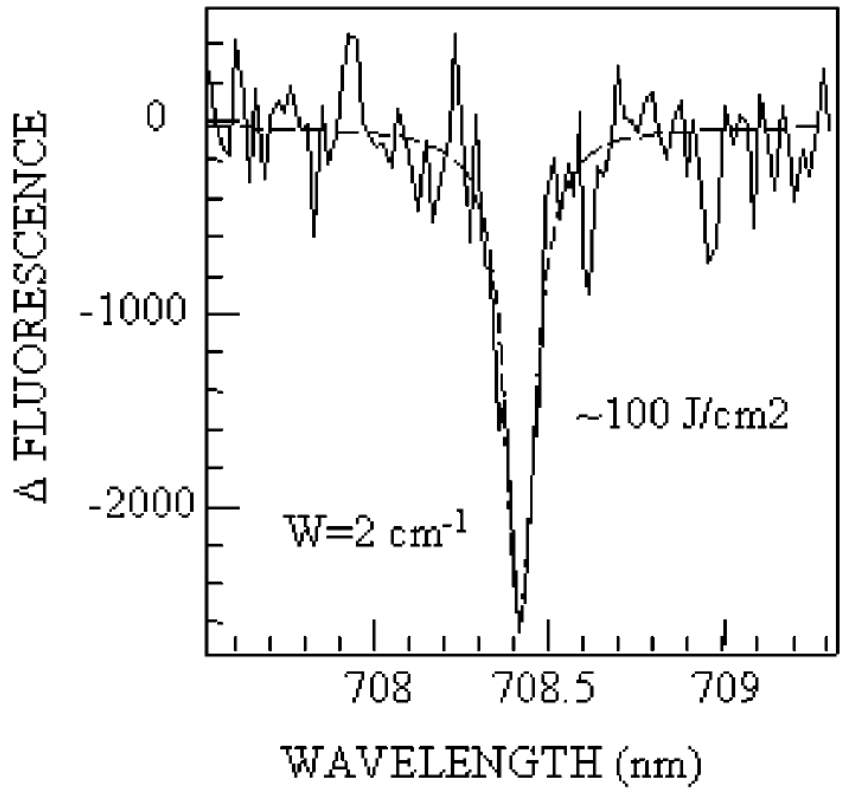

Figure 3.

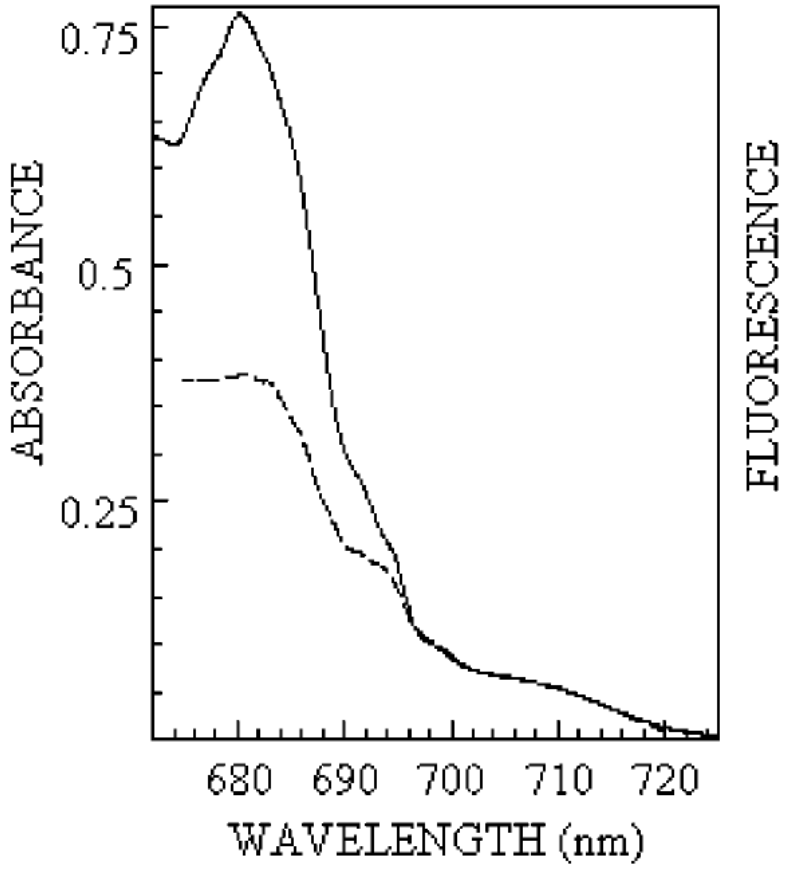

Figure 4.

CHAPTER 3. EMISSION SPECTRA OF SINGLE MOLECULE PHOTOSYSTEM I COMPLEXES FROM CYANOBACTERIUM SYNECHOCYSTIS PCC 6803

A paper submitted to Photosynthetic Research* with coauthors:

Tse-Ming Hsin, Tõnu Reinot, Kerry Riley, and Valter Zazubovich

Abstract

Emission spectra of individual trimeric photosystem I complexes from cyanobacterium *Synechocystis* PCC 6803 were measured. Broad structureless bands are peaked at approximately 720 nm, indicating strong electron-phonon coupling for the lowest-energy red antenna state (C714), in agreement with spectral hole burning results. No sharp lines belonging to the higher-energy (C708) state were observed in emission spectra, which suggest that the two red antenna states (C708 and C714) are connected by relatively fast and effective energy transfer. The results are compared with those obtained for photosystem I from *Synechococcus elongatus* (Jelezko et al. 2000); possible origins of narrow zero-phonon lines (ZPL) observed by Jelezko et al. in emission spectra of PSI from *Synechococcus* near 711-712 nm are discussed.

---

* After extensive modifications and after additional data were obtained, the work was published in Journal of Physical Chemistry B **2007,** 111(1), 286-292.

Introduction

Photosystem I (PSI) is one of the two major photosystems involved in oxygenic photosynthesis and the largest and most complex membrane protein for which detailed structural and functional information is now available.[1,2] It converts light energy into chemical energy by transferring electrons through the thylakoid membrane from lastocyanine or cytochrome c_6 to $NADP^+$. Structures of PSI from the cyanobacterium *Synechococcus elongatus*[2] and higher plant (*Pisum sativum*)[3] were recently determined with high resolution by means of X-ray diffraction. Similarity of the core structures indicates that only minor variations in the core organization and function occurred in the way of evolution and provides a legitimate reason to believe that PSI cores from other organisms are also similar. (PSI of higher plants, deep-water strains of *Prochlorococcus marinus*,[4] as well as some other cyanobacteria grown under iron[5,6] additionally contains peripheral light-harvesting complexes.) Therefore, cyanobacterial PSI can serve as a good model for the PSI core of higher plants. Cyanobacterial PSI has a trimeric structure,[2] with each monomer being a complex network of chlorophyll *a* (Chl *a*) molecules embedded into protein where ~90 antenna Chls surround the "reaction center" (containing primary electron donor P700 and accessory Chls) and funnel the sunlight energy into it. While the majority of antenna Chls absorb at 670-690 nm, some absorb at even longer wavelengths than the strongly coupled reaction center dimer, P700.[7,8] It has been shown that these "red antenna states" are localized on aggregates of Chls (closely spaced and strongly coupled), rather than on single Chl *a* molecules with peculiar interactions with their protein environment. Three red antenna states (C708, C715, C719) were resolved in case of *Synechococcus*[9] and two (C708 and C714) in case

of *Synechocystis* PCC 6803.[8,10] Spectral hole burning (SHB) experiments[8,9,11] showed that the properties of the red-most antenna states of *Synechococcus* (C719) and *Synechocystis* (C714) PSI are almost identical, suggesting that very similar aggregates are responsible for those states, while the difference in the peak wavelength is due to small differences in protein environment. Also, strong electron-phonon coupling, large permanent dipole moment change, and large rate of pressure-induced shift of spectral holes (lines) indicate that the electron exchange contributes significantly to the excitonic coupling of the C714 and C719 aggregates. Spectral hole burning (SHB) is a powerful frequency domain technique for the study of the $S_1(Q_y)$ excited state electronic structure, excitation energy transfer (EET) and electron transfer (ET) dynamics of protein-chlorophyll (Chl) complexes at low temperatures. However, despite its frequency selectivity, SHB still probes ensembles of complexes, which are in some sense inhomogeneous. This is manifested, for example, by broadening of spectral holes in external fields.[12] Single photosynthetic complex spectroscopy (SPCS) allows investigating the properties of the complexes one by one, therefore removing inhomogeneity-related effects. While significant progress has been achieved in the spectroscopic studies of single LH-2 complexes[13-19] as well as LH-1[20,21] and LHC-II[22] complexes, there is only very limited single complex data available for PSI. The only work we are aware of is the paper on *Synechococcus* PSI[23] and its derivatives. Undoubtedly, the lack of published results is due to the complexity of PSI. As mentioned above, there are almost 300 Chls per PSI trimer (i.e. almost 300 spectral lines in a relatively narrow wavelength range). Further, PSI does not possess the high symmetry of light harvesting complexes from purple bacteria, which reduces the number

of lines observable in the spectra of those complexes. Jelezko et al. focused exclusively on the red antenna state region of PSI from *Synechococcus*; their results confirmed that the lowest-energy state (C719) is indeed characterized by very strong electron-phonon coupling. On the other hand, their observation of narrow zero-phonon lines near 711-712 nm, most likely belonging to higher-energy red state (C708) of *Synechococcus*, present in both emission and fluorescence excitation spectra seems to indicate that different red antenna states are not connected by energy transfer. The latter conclusion, however, contradicts the fluorescence anisotropy data,[7] which suggests that the C708→C719 energy transfer in *Synechococcus* does occur. It also contradicts our observation of the C708→C714 energy transfer for *Synechocystis*,[11] if one assumes, of course, that the structures of PSI are similar for the two cyanobacteria. In this manuscript we will describe single complex emission spectra of the PSI from *Synechocystis*. As mentioned above, *Synechocystis* PSI possesses two different red antenna states, which makes interpretation of results somewhat easier than in case of *Synechococcus*. [Note that the authors of some works (ref. 24 and references therein) were unable to resolve all the red states distinguishable with the SHB and continued to use smaller number of red pigment pools in their analysis.] Results presented in this manuscript show no support for more than one emitting state, in agreement with SHB results,[11] indicating that energy transfer does occur from the C708 to the C714 (emitting) state.

Experimental Section

Wild-type trimeric PSI complexes were extracted as described in ref. 8. The concentrated samples from the same batch as used in earlier hole burning experiments[8,11] were first dissolved in buffer (10 mM MOPS, 0.05% β-dodecylmaltoside, pH = 7.0) to achieve the $OD_{680} \approx 0.4$ per 1 cm thickness. (That corresponds to Chl concentration of approximately 10^{-5} M, i.e. to trimeric PSI concentration smaller than 10^{-7} M.) This solution was further dissolved ~1000 times in buffer/glycerol mixture (3:1) and spin-coated on a plasma-cleaned sapphire plate yielding a film thickness of less than 1 μm. The use of glycerol is not meant to facilitate formation of a transparent glass, but merely to adjust the viscosity of the solution for better thin film formation. We do not use polymers for sample preparation since we believe that the photosynthetic complexes embedded in dry polymer films are relatively more disrupted than in typical bulk experiments. The sample was quickly placed into the cryostat, providing a cold (< 0º C) dark environment, and then frozen to liquid helium temperature in about 20 minutes. All sample handling procedures were performed in dim light to avoid sample degradation. The optical setup was based on a home-built confocal microscope with Newport 60× 0.85 NA objective attached to the sample holder inside the cryostat (Janis). In order to reduce sample movements due to temperature expansion, the rod of the sample holder was made from fused quartz. The sample was moved in relation to the objective along the objective axis using an electromagnet with two parallel coils, one superconducting (for T < 7K) and the other made of copper wire. Moving the focal spot across the sample was achieved by using a scanning mirror. Excitation was performed with a Coherent 699 laser with Exciton LD-688 dye (660-720 nm) and with intra-cavity etalons

removed (line width several GHz). After the adjustment, ensuring that the PSI-containing film was indeed in the focal plane of the objective, the mirror was scanned while the fluorescence (excited at 675-680 nm) was collected (λ > 700 nm) by the avalanche photodiode (Perkin-Elmer, dark count < 25 s^{-1}). An example of the resulting "raster-scan" image is presented in the Figure 1. Afterwards the mirror was moved to positions determined from that image, in order to focus on different single complexes, and spectroscopic measurements were performed. Emission spectra were measured with Princeton Instruments PI-MAX II generation intensified CCD camera through Omega AELP 700 long-pass filter (and DRLP 710 dichroic mirror) and Jobin-Yvon Triax 320 spectrometer with resolution of 0.4 nm. Excitation was typically at 675-680 nm. Excitation intensities (adjusted using neutral filters, LOMO) are given in the following subsections and in the figure captions. A short-pass filter (Omega; 3rd Millennium SP700) was placed just after the laser power stabilizer (CRI) in order to suppress broadband dye fluorescence and thereby reduce background.

Results and Discussion

The bulk emission spectrum of trimeric PSI from *Synechocystis* (not shown) peaks at 720 nm. This value is similar to those reported in ref. 8 and 25. No shoulders were observed at shorter wavelengths. Quality of the bulk absorption spectrum was checked and the shape of the spectrum was in agreement with that reported in ref. 8 and 11. Figure 2A represents the typical low temperature emission spectrum of a single PSI complex from *Synechocystis*. The spectrum is peaked at 720 nm and is quite broad and structureless. (The diagram of the emission band maximums of 27 single complexes is

shown in the Figure 2B.) This is in agreement with the spectral hole burning results[8,26] and indicates that electron-phonon coupling for the emitting (C714) state is very strong. Strong coupling (total Huang-Rhys factor S ≈ 2), along with possible light-induced spectral diffusion, is the reason why ZPLs belonging to this state are not observable. A similar result was reported for the lowest energy red antenna state of *Synechococcus* (C719).[23] However, unlike in ref. 23, we did not observe any sharp lines near 710 nm, where direct emission from the C708 state might be expected. Therefore, we conclude that the red antenna states in *Synechocystis* are connected by efficient energy transfer, in agreement with spectral hole burning results.[11] At this point it may be asked if the above finding suggests that there is actually only one red antenna state in *Synechocystis*, as proposed in ref. 24. We consider it unlikely. First, as demonstrated in ref. 8 and 26, electron-phonon coupling clearly changes across the red antenna absorption band, becoming significantly weaker at 706-710 nm (S ≤ 1.2) than at 714-718 nm (S ≈ 2). The same is true also for the permanent dipole moment difference between excited and ground state.[8] We are unaware of a theoretical model that would explain about two times variation of these parameters within the inhomogeneously broadened band belonging to a single aggregate. In the case of a (positive) correlation between electron-phonon coupling and the peak wavelength for a single lowest state, emission from PSI with the lowest state ZPL at 706-710 nm is expected at about 708-712 nm (due to weaker electron-phonon coupling, S ≈ 1.2), contrary to single complex spectroscopy results presented in this work (See Figure 2B) and to bulk emission spectra.[8,25] It is interesting to consider the implications of the above discussion to the results obtained by Jelezko et al. for *Synechococcus* PSI.[23] The distribution of narrow ZPLs in the

fluorescence excitation spectra observed in ref. 23 peaks at 711-712 nm. Assuming weak to moderate electron-phonon coupling,[9,23] respective absorption maximum should be at 709-710 nm in the bulk spectra, i.e. the lines observed by Jelezko et al. most likely belong to the C708 state. Emission maximum for this state (in the absence of the lower-energy states) is expected at about 713-714 nm. In single complex emission spectra the total intensity of the C719 emission (peaked at 730 nm) is much higher than that of the C708 emission, although bulk absorption is comparable. Also, no significant shoulder near 713 nm is observed in bulk emission spectra. Thus, all data suggest that emission from the C708 upon high-energy (indirect) excitation is relatively weak (if it is present at all). On the other hand, upon direct excitation (fluorescence excitation mode) sharp lines belonging to the C708 state were detectable, even though the setup design did not favor the detection of the ~713 nm emission (filter transmitting at $\lambda > 725$ nm). There are two possible explanations for the presence of narrow C708 lines in emission spectra of single PSI of *Synechococcus*. In the first scenario, the C708→C719 energy transfer is unlikely and upon excitation of the C708 it emits by itself with the yield so high that Jelezko et al. were able to detect sharp C708 lines near 711-712 nm in fluorescence excitation spectra with a filter transmitting at $\lambda > 725$ nm. Relative weakness of the C708 emission upon indirect excitation may be explained by peripheral location and/or unfavorable orientation of the C708 aggregate, i.e. energy rarely gets transferred from bulk antenna downward to the C708 aggregate. Thus, in this scenario it seems plausible that the C708 state of PSI from *Synechococcus* originates from the B31/B32/B33 trimer, not present in *Synechocystis* since the histidine residue coordinating these chlorophylls is absent.[27] Other strongly coupled aggregates on the periphery of

the complex are A12/A14, A10/A18, B09/B17 and A33.[27,28] However, the site energies of these chlorophylls,[28] except A14, are incompatible with them being the origin of the red antenna states. Other candidates proposed for the strongly coupled dimers are B07/A32, A38/A39 and B37/B38,[29] A24/A35 and B22/B34,[27] A27/A28 and B24/B25[28] or B02/B03 and A03/A04.[29,30] However, these dimers are situated closer to the center of the complex and are unlikely to be avoided by energy transfer. Thus, in this scenario, none of the above dimers is likely to contribute to the C708 state. On the other hand, an alternative explanation is also possible, with the energy transfer from C708 to C719 not just possible but likely and with the C708 (and C715) state functioning as an emitting trap only while the lowest trap is unavailable for downward energy transfer, for example while C719 is excited ($\tau_{fluor} \approx 2$ ns). If the PSI complex was on the edge of saturation, then within the collection time of the emission spectra (60 sec)[23] many multiple excitation events could occur, resulting in the weak C708 emission in addition to the strong C719 emission. Note that Jelezko et al. focused as much as 30 μW on a single PSI complex (i.e. about 3 kW/cm^2) during their emission spectra measurements.[23] The latter power density was approximately 600 times larger than used in their fluorescence excitation measurements (50 nW).[23] Thus, saturation/multiple excitation regime was quite likely. Upon both resonant and non-resonant excitation the C708 state more often than not transfers energy downward to the C719 state, and emission occurs from the latter state, leading to more easily detectable fluorescence at wavelengths longer than 725 nm. If this explanation is right, the relative intensity of the C708 ZPLs in the single complex emission spectra should depend on excitation intensity. Research in progress on PSI of both *Synechocystis* and *Synechococcus* should provide answers to the questions raised in

this manuscript.

References

1. Fromme, P.; Mathis, P. *Photosynth. Res*. **2004**, *80*, 109.
2. Jordan, P.; Fromme, P.; Witt, H. T.; Klukas, O.; Saenger, W.; Krauss, N. *Nature* **2001**, *411*, 909.
3. Ben-Shem, A.; Frolow, F.; Nelson, N. *Nature* **2003**, *426*, 630.
4. Bibby, T. S.; Nield, J.; Partensky, F.; Barber, J. *Nature* **2001**, *413*, 590.
5. Bibby T. S.; Nield, J.; Barber, J. *Nature* **2001**, *412*, 743.
6. Boekma, E. J.; Hifney, A.; Yakushevska, A. E.; Piotrowsky, M.; Keegstra, W.; Berry, S.; Michel, K.-P.; Pistorius, E. K.; Kruip, J. *Nature* **2001**, *412*, 745.
7. Pålsson, L.-O.; Dekker, J. P.; Schlodder, E.; Monshouwer, R. van Grondelle, R. *Photosynth. Res.* **1996**, *48*, 239.
8. Ratsep, M.; Johnson, T. W.; Chitnis, P. R.; Small, G. J. *J. Phys. Chem. B* **2000**, *104*, 836.
9. Zazubovich, V.; Matsuzaki, S.; Johnson, T. W.; Hayes, J. M.; Chitnis, P. R.; Small, G. J. *Chem. Phys.* **2002**, *275*, 47.
10. Melkozernov, A. N.; Lin, S.; Blankenship, R. E.; Valkunas, L. *Biophys. J.* **2001**, *81*, 1144.
11. Hsin, T.-M.; Zazubovich, V.; Hayes, J. M.; Small, G. J. *J. Phys. Chem. B* **2004**, *108*, 10515.
12. Kohler, M.; Friedrich, J.; Fidy, J. *Biochem. Biophys. Acta* **1998**, *1386*, 255.
13. Hofman, C.; Ketelaars, M.; Matsushita, M.; Michel, H.; Aartsma, T.; Kohler, J. *Phys.*

*Re*V. *Lett*. **2003**, *90*, 13004.

14. Hofman, C.; Aartsma, T.; Michel, H.; Kohler, J. *Proc. Natl. Acad. Sci. U.S.A.* **2003**, *100*, 15534.
15. Ketelaars, M.; Matsushita, M.; van Oijen, A. M.; Kohler, J.; Aartsma, T. J.; Schmidt, J. *Biophys. J.* **2001**, *80*, 1591.
16. Matsushita, M.; Ketelaars, M.; van Oijen, A. M.; Kohler, J.; Aartsma, T. J.; Schmidt, J. *Biophys. J*. **2001**, *80*, 1604.
17. Tietz, C.; Chekhlov, O.; Drabenstedt, A.; Schuster, J.; Wrachtrup, J. *J. Phys. Chem. B* **1999**, *103*, 6328.
18. van Oijen, A. M.; Ketelaars, M.; Kohler, J.; Aartsma, T. J.; Schmidt, J. *Chem. Phys*. **1999**, *247*, 53.
19. van Oijen, A. M.; Ketelaars, M.; Kohler, J.; Aartsma, T. J.; Schmidt, J. *Biophys. J.* **2000**, *78*, 1570.
20. Gerken, U.; Jelezko, F.; Gotze, B.; Branschadel, M.; Tietz, C.; Ghosh, R.; Wrachtrup, J. *J. Phys. Chem*. *B* **2003**, *107*, 338.
21. Ketelaars, M.; Hoffman, C.; Kohler, J.; Howard, T. D.; Cogdell, R. J.; Schmidt, J.; Aartsma, T. J. *Biophys. J.* **2002**, *83*, 1701.
22. Tietz, C.; Jelezko, F.; Gerken, U.; Schuler, S.; Schubert, A.; Rogl, H.; Wrachtrup, J. *Biophys. J.* **2001**, *81*, 556.
23. Jelezko, F.; Tietz, C.; Gerken, U.; Wrachtrup, J.; Bittl, R. *J. Phys. Chem*. *B* **2000**, *104*, 8093.
24. Gobets, B.; van Stokkum, I. H. M.; van Mourik, F.; Dekker, J. P.; van Grondelle, R. *Biophys. J*. **2003**, *85*, 3883.

25. Gobets, B.; van Amerongen, H.; Monshouwer, R.; Kruip, J.; Rogner, M.; van Grondelle, R.; Dekker, J. P. *Biochem. Biophys. Acta* **1994**, *1188*, 75.

26. Hayes, J. M.; Matsuzaki, S.; Ra¨tsep, M.; Small, G. J. *J. Phys. Chem. B* **2000**, *104*, 5625. Sener, M. K.; Lu, D.; Ritz, T.; Park, S.; Fromme, P.; Schulten, K. *J. Phys. Chem. B* **2002**, *106*, 7948.

27. Damjanovic, A.; Vaswani, H. M.; Fromme, P.; Fleming, G. R. *J. Phys. Chem. B* **2002**, *106*, 10251.

28. Balaban, T. S. *FEBS Lett.* **2003**, *545*, 97. Erratum *FEBS Lett.* **2003**, *547*, 235.

29. Byrdin, M.; Jordan, P.; Krauss, N.; Fromme, P.; Stehlik, D.; Schlodder, E., *Biophys. J.* **2002**, *83*, 433.

30. Balaban, T. S. Private communication.

Figure Captions

Figure 1: Image of the thin film containing single PSI complexes (red peaks) obtained using avalanche photodiode by varying the orientation of the scanning mirror. Complexes were excited with 250 nW at 680 nm and fluorescence was collected at $\lambda >$ 700 nm. T = 10 K.

Figure 2: Frame A: Typical emission spectrum of a single PSI complex from *Synechocystis* excited at 675 nm. Approximately 1.5 μW was focused on the single complex and the collection time was 300 seconds. T = 10 K. Frame B: Histogram of the emission band maximum wavelengths based on the data from 27 single PSI complexes. Excitation was at 675 nm.

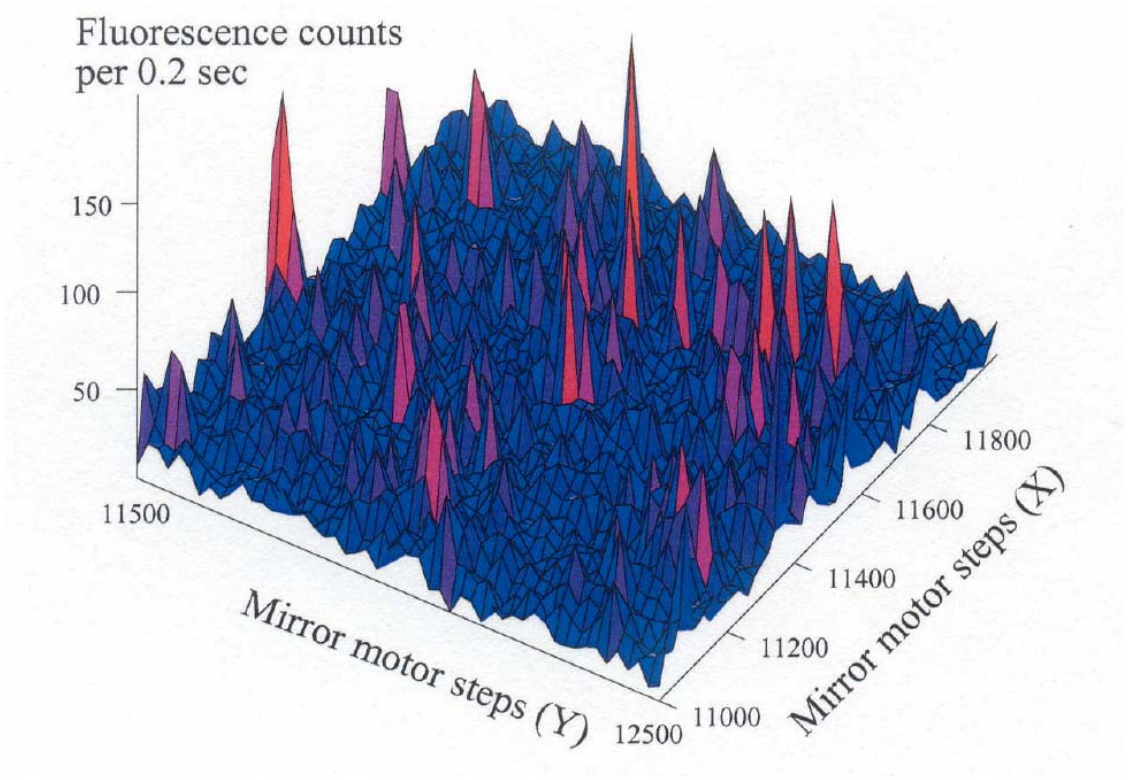

Figure 1.

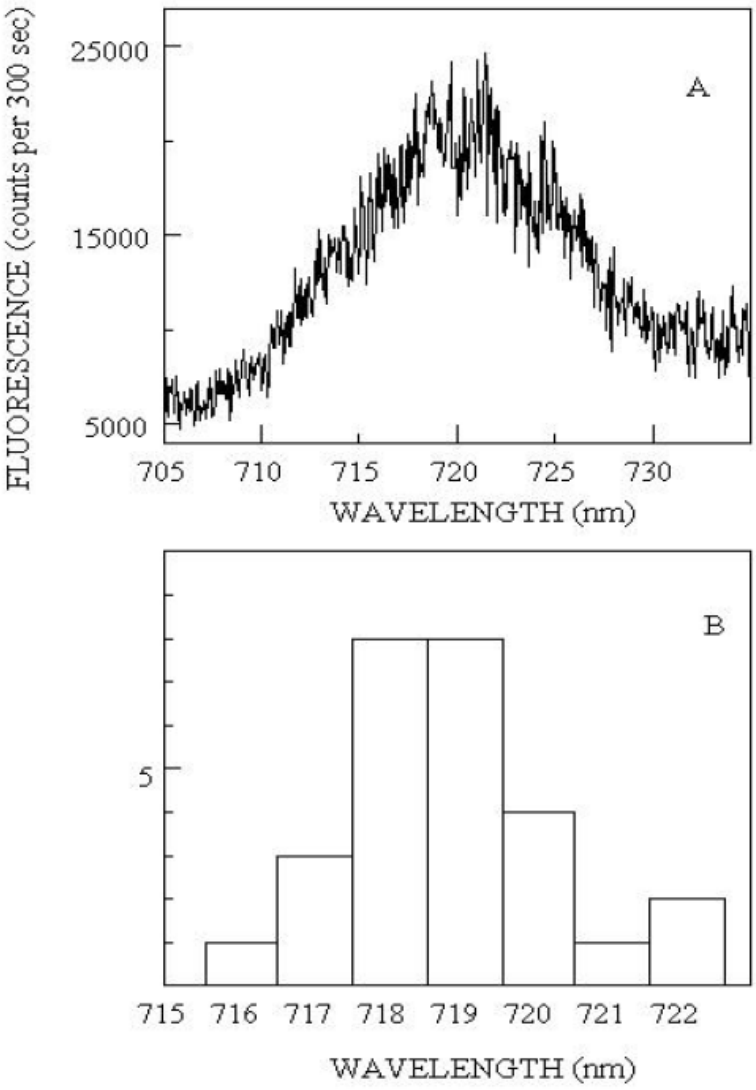

Figure 2.

CHAPTER4. ULTRAFAST VIBRATIONAL EVOLUTION OF EXCITED-STATE COUMARIN 153 USING FS/PS CARS AS A TRANSIENT RAMAN PROBE

A Paper published in Femtochemistry VII:

Fundamental Ultrafast Processes in Chemistry, Physics, and Biology*

B. D. Prince, A. Chakraborty, B. M. Prince, T.-M. Hsin, and H. U. Stauffer

1. INTRODUCTION

The development of techniques to study molecular vibrations with reasonable frequency resolution in the femtosecond time regime for excited state molecules has opened new avenues of research for the understanding of molecular structure following electronic excitation. Frequency resolution allows one to observe directly the evolution of vibrational modes as a function of some relevant time delay without the need to apply Fourier Transform techniques or to separate complicated beat patterns to determine pairs of involved modes. Here, vibrational evolution upon electronic excitation in coumarin 153 (C153) is observed using a transient Raman probe technique developed in our laboratory that is a variation of time-resolved coherent anti-Stokes Raman spectroscopy (TR-CARS). The technique, named fs/ps CARS, is described in detail elsewhere.[1] C153

---

* Reprint with permission from Femtochemistry VII: Fundamental Ultrafast Processes in Chemistry, Physics, and Biology **2006,** 66-69

has been extensively studied for its ideal solvatochromic properties upon excitation that allow it to be used as a probe for solvent reorganization. However, despite the wealth of work done on the solvation properties, only a few studies have been undertaken to understand the molecular changes of the solute molecule upon electronic excitation.

2. EXPERIMENTAL

A Ti:Sapphire laser system generates pulses of ~50 fs duration centered at 800 nm with a repetition rate of 1 kHz and power of 2.1 mJ/pulse. Part of the 800 nm pulse is used to generate visible pulses at frequencies ω_1 and ω_2 via optical parametric amplification and frequency mixing.[1] The residual 800 nm beam is split to generate a narrowband (ω_3, $\Delta\omega$ ~16 cm^{-1}) ps-duration probe pulse centered at 795 nm and a pump pulse (ω_{pump}) near 400 nm via frequency doubling.

The visible fs/ps beams are chosen to be centered at ω_1 = 509 nm (19646 cm^{-1}) and ω_2 = 555 nm (18018 cm^{-1}). After excitation by ω_{pump} ($S_1 \leftarrow S_0$), the ω_2 pulse is resonant with the ground electronic state (stimulated emission, $S_1 \rightarrow S_0$). ω_1 is time overlapped with ω_2 and repopulates the electronic excited state from the transition caused by ω_2 ($S_0 \leftarrow S_1$) (Fig. 1).

The three beams associated with the fs/ps CARS probe scheme (ω_1, ω_2, and ω_3) are aligned in a folded BOXCARS arrangement, and the spatially-filtered output signal is focused into a spectrometer (Ocean Optics, USB-2000, ~0.7 nm resolution). This scheme generates vibrationally resolved spectra of Raman active modes while maintaining sub-picosecond temporal resolution associated with time-resolved CARS. The delay of the pump beam, which is aligned to be collinear with the ω_3 pulse, is adjusted via a

computer-controlled translation stage. The resultant spectra are fit to Lorentzian lineshapes, and statistical information (intensity, peak frequency, FWHM, *etc*.) is generated and plotted against pump delay.

C153 was used as purchased from Exciton and was dissolved in commercially available solvents for study in these experiments. The solvents include the hydrogen bonding solvents methanol (MeOH) and butanol (BuOH) and non-hydrogen bonding solvent acetonitrile (ACN). The samples were diluted to a concentration of 8 mM. Samples were placed in a 220 μm thick rotating home-built cell to ensure the sample is refreshed between laser shots.

3. RESULTS AND DISCUSSION

Figure 2 displays data typical of our experimental setup. The excited state spectra (top graphs) are generated at a fixed excitation pump pulse delay (~30 ps for Fig. 2) and have been corrected to remove signal resulting from the ground state (lower graphs). The evolution of the Raman vibrational spectrum from ~1000-2000 cm^{-1} is monitored with the excitation pump delay and evolution of the modes can be followed within the time resolution (~100 fs) of our experiment. At long delays (~15 ps), the two solvents differ considerably in the peak position of the mode nearest 1700 cm^{-1}. In MeOH, the position is detected at approximately 1671 cm^{-1}, while in ACN the position is near 1690 cm^{-1}. The focus of the results here will be on the peaks denoted as “A” and “B” in the top panels of Fig. 2.

The 1584 cm^{-1} frequency (Fig. 3) shows some time dependent shift in MeOH, but this shift is either absent in ACN or considerably faster than the time resolution of this

setup. To determine whether this time dependent evolution is related to solvent response or to simple molecular evolution, another solvent (butanol) was chosen whose solvation dynamics are considerably slower than the two studied thus far.[2] The frequency evolution in BuOH is similar to that in MeOH but on a considerably slower timescale (3.6 ps vs. ~20 ps). This suggests that this frequency is related to the evolution of a longer term timescale of solvation. According to previous work by Maroncelli and co-workers, the solvation dynamics of C153 in ACN occurs considerably faster than MeOH, which in turn occurs faster than BuOH.[2] Further studies on the nature of this shift are currently under way in our laboratory.

Previous work on coumarin 102 (C102), similar in structure to C153, has defined the free C=O stretch in the region of 1730-1740 cm^{-1} in the excited state.[3] Thus it is not expected that the excited state mode observed near 1670 cm^{-1} in the alcohols and near 1690 cm^{-1} in the ACN solution is the direct C=O stretch; however, it is potentially a combination mode involving the skeletal motions and a C=O stretch component. Kiefer and coworkers have calculated and assigned the modes of coumarin 152 (C152), which is closely related to C153, in the ground state and compared to experimentally measured Raman spectra in solid and liquid phases.[4] A ground state mode observed at 1603 cm^{-1} contains a C=O stretch component in C152. This agrees with the slight difference observed in the solution phase for this mode in the ground state in our measured C153 spectra (1599 *vs*. 1603 cm^{-1}, Fig. 2, bottom panels). Thus, it is expected that the excited state the mode near 1690 cm^{-1} has some relationship to a C=O stretch and further details regarding the behavior of this peak will be addressed elsewhere.

REFERENCES

1. Prince, B. D.; Chakraborty, A.; Prince, B. M.; Stauffer, H. U. *J. Chem. Phys.* **2006,** *125*, 044502.
2. Horng, M.L.; Gardecki, J.A.; Papazyan, A.; Maroncelli, M. *J. Phys. Chem.* **1995,** *99*, 17311.
3. Nibbering, E.T.J.; Tschirschwitz, F.; Chudoba, C.; Elsaesser, T. *J. Phys. Chem. A* **2000,** *104*, 4236.
4. Vogel, E.; Gbureck, A.; Kiefer, W. *J. Mol. Struct.* **2000,** *550*, 177.

Figure Captions

Figure 1: Left: Experimental pulse scheme utilized in this fs/ps CARS experiment. An initial pump beam excites population from $S_0 \leftarrow S_1$, where two broadband time overlapped beams ω_1 and ω_2 prepare population in excited state Raman vibrational modes after some time delay. A final ps narrowband probe beam ω_3 then probes population and a fourth wave is detected. Right: Chemical structure of C153 and emission of C153/MeOH upon 400 nm excitation.

Figure 2: Ground (bottom) and excited state (top) fs/ps CARS spectra of C153 in two solvents: MeOH (left) and ACN (right). Solvents are noted with the "*" symbol. Particular attention is spent on "Peak A" and "Peak B" in this experiment. Excited state spectra are generated with the pump pulse fixed at a long time delay (tens of ps). Note the large frequency difference of "Peak A" in both solvents.

Figure 3: Central peak frequency evolution of "Peak B" (~1584 cm^{-1}) in the excited state spectra of C153 in three solvents. The evolution of this mode appears to be solvent dependent rather than purely molecular in nature. The timescales of evolution fit well to single exponentials and appear to be related to slower timescales of solvation.

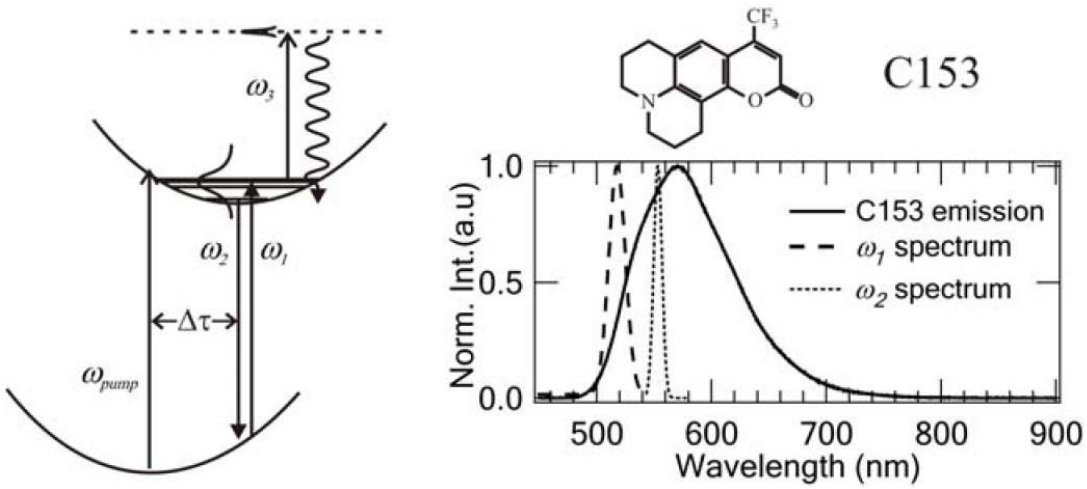

Figure 1.

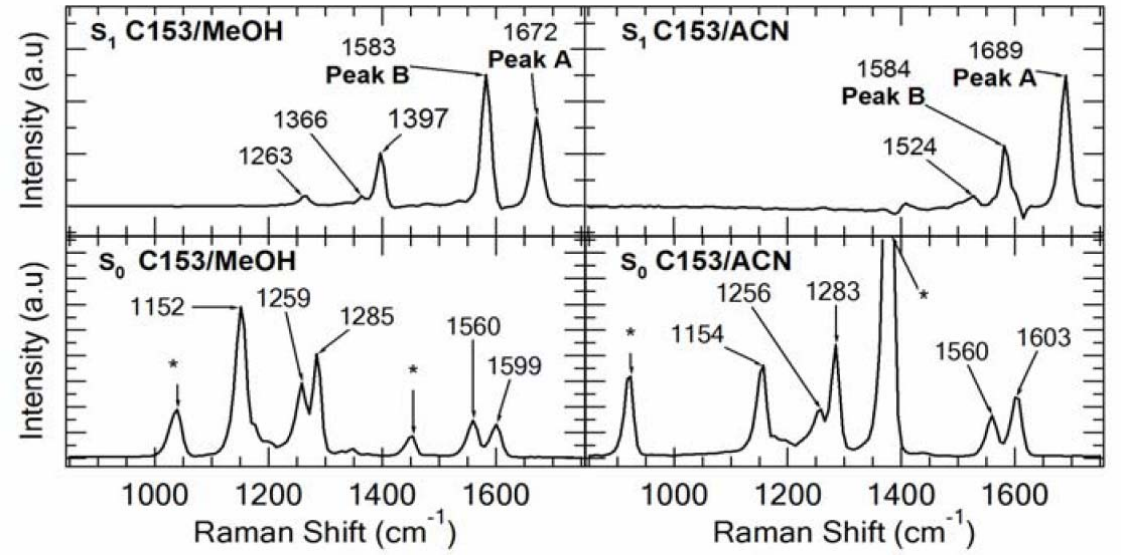

Figure 2.

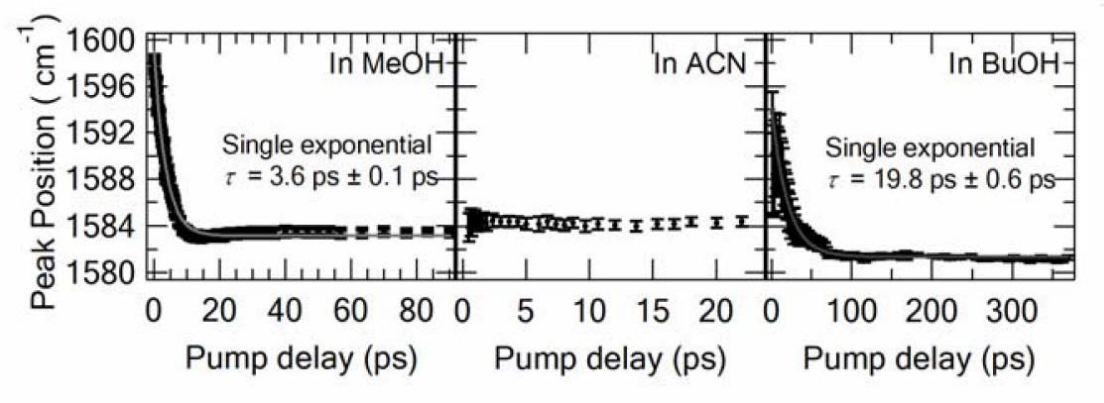

Figure 3.

CHAPTER 5. SINGLE MOLECULE REACTIONS IN LIPOSOMES

A paper submitted Journal of the American Chemical Society

Tse-Ming Hsin and Edward S. Yeung

Abstract

To eliminate any potential influences from surfaces, orientations and steric effects, the reaction of single alkaline phosphatase molecules from bovine intestinal mucosa is studied inside liposomes. Fluorescent images of individual TOTO-3-labeled proteins in the liposomes provide direct proof of having one and only one enzyme molecule in each reaction. Electrofusion of the enzyme-containing liposome with the substrates-containing liposome initiates the enzymatic reaction. After incubation, the products of the reaction are quantified by calibration against liposomes with known concentrations of fluorescein to reveal the reactivity of individual protein molecules. Individual molecules of the enzyme show a wide range of activities which span from tens to several hundreds of molecules/second. The distribution of reaction rates of these molecules is non-Gaussian and appears to contain two maxima plus a few molecules of higher activity. The heterogeneity in activity indicates structural variations of the protein. Besides glycoforms, phosphate-induced structural change at the active site of this enzyme is one of the major reasons which account for the ~20-fold variation in activities.

Introduction

In the early 1850s, scientists started to study the kinetics of catalytic reactions of biomolecules.[1] For more than a century, chemical reactions are always studied on ensembles of

molecules. Important parameters such as reaction rate and rate constant, both statistical concepts, were then formulated. With the advancement of instrumentation, scientists can now study reaction kinetics[2-7] and dynamics[8,9] at the level of single molecules. Information such as the stochastic behavior of molecular reactivity is no longer hidden behind bulk experiments. For example, detection of single-molecule activity of lactate dehydrogenase[3,4] and alkaline phosphatase[5,10] have been reported. The fluorescent products of single enzyme molecules can be detected by laser-induced fluorescence in a narrow capillary after electrophoretic migration. The activation energy and rate constant for individual molecules are thus characterized.

In order to mimic biochemical transformations in living systems, biomolecular reactions have also been carried out in the "artificial cells"—liposomes, which are vesicles with membranes composed of lipid bilayers.[11-15] The artificial vesicle creates a lipid boundary which provides a cell-like environment for biomolecules. In these studies, liposomes also serve as ultrasmall biomimetic containers for the reactants. Several manipulation techniques such as electrofusion,[11-13] electroinjection[14, 15] and light-induced fusion,[16] have been used to initiate the reactions. Various types of reactions such as intercalation of dye and DNA molecules,[13] catalytic reactions of enzymes,[14,15] and hydrogel formation by reacting a polymer with metal ions[17] have been reported.

Here we demonstrate, for the first time, the reaction of single enzyme molecules in liposomes. The enzyme, alkaline phosphatase (ALP), is confined in a vesicle and the substrate, fluorescein diphosphate (FDP), is confined in another one. The contents of the liposomes are brought together by electrofusion. The single-molecule enzymatic reaction produces fluorescein (F) molecules, which are detected by fluorescence microscopy. The presence of one and only one enzyme molecule is confirmed by direct observation and the reaction rate is deter-

mined accurately with the aid of calibration standards. Unlike previous reports, the enzyme molecule is kept in solution and away from the walls of the container throughout the reaction.

Experimental Section

Chemicals and Materials. Trizma base, alkaline phosphatase from bovine intestinal mucosa, magnesium chloride, and phosphatase inhibitor cocktail 1 were obtained from Sigma-Aldrich (St. Louis, MO). Fluorescein diphosphate, silicone isolator, and TOTO-3 iodide were obtained from Invitrogen (Carlsbad, CA). Chloroform and methanol were purchased from Fisher Scientific (Pittsburgh, PA). Soybean L-α-phosphatidylcholine (Soybean PC) was obtained from Avanti Polar Lipids (Alabaster, AL). Slide-A-Lyzer analysis cassettes and Halt phosphatase inhibitor cocktail were purchased from Pierce (Rockford, IL). Amine-coated coverslips were purchased from Telechem International (Sunnyvale, CA). PVDF membranes (1,000,000 MWCO) was obtained from Spectrum Labs (Rancho Dominguez, CA)

Liposome Preparation and Protein Labeling. Soybean PC liposomes were prepared by the rotary evaporation method.[11-13,18] Typically, 15 µL of 133 mM soybean PC, 985 µL of chloroform, and 100 µL of methanol were mixed with 2 mL of aqueous solution containing the molecules of interest. The mixture was heated to 41 ºC (Precision, Model 281) under reduced pressure (Brinkmann, Model B-169) and the organic phase was removed in 2-3 min. The aqueous phase then became cloudy and liposomes were formed. The cloudy solution was dialyzed extensively to remove reactants outside of the liposomes. The intracellular buffer for both FDP-containing and ALP-containing liposomes was 10 mM Trizma base and 1 mM $MgCl_2$ (pH 9.7). The FDP concentration was 10 µM and the ALP concentration was 25.6 pM for the single-molecule experiments. For protein labeling, TOTO-3 iodide was used to label alkaline

phosphatase molecules. TOTO-3 (solution in DMSO) was first diluted 100 times by the buffer mentioned above. 32.6 µL of the 100-fold diluted dye solution was mixed with 46.6 µL of 2.2 nM ALP. The intracellular buffer was added to make a final volume of 2 mL and the mixture was transferred to the round-bottom flask for rotary evaporation. Both of the absorption and emission maxima of TOTO-3 iodide and of fluorescein are separated by ~150 nm. Therefore, the dye-labeled enzymes would not interfere with fluorescence registration of the products.

Microscopy and Manipulation. Fig. 1 shows the experimental setup which consists of an inverted microscope (Zeiss Axiovert 100 TV, Carl Zeiss MicroImaging, Inc., Thornwood, NY), two 3-D translation stages (PT3, Thorlabs, Newton, NJ) for positioning carbon fiber microelectrodes (Carbostar-1, Kation Scientific, Minneapolis, MN), two visible lasers for fluorescence excitation, one near-IR diode laser for optical trapping,[11-13,19] and an intensified-CCD camera (GenIV, Princeton Instruments, Fenton, NJ). The 488-nm line from an argon-ion laser (2211-10GLYVW, Uniphase, Milpitas, CA) was used to excite fluorescein; the 632.8-nm line from a He-Ne laser (NT55-473, Uniphase) was used to excite TOTO-3-labeled proteins. The 808-nm beam from the near-IR laser diode (QFLD-808-100S, QPhotonics, Chesapeake, VA) was collimated and shaped for optical trapping of the liposomes. A polychroic mirror (FF500/646-Di01, Semrock, Rochester, NY) and a dual-notch filter (NF01-488/635, Semrock, Rochester, NY) were employed to work with the lasers. An oil-immersion 100× microscope objective (EC Plan-Neofluar Carl Zeiss MicroImaging, Thornwood, NY) was used for imaging and trapping.

Carbon fiber microelectrodes and optical tweezers were used to manipulate and electrofuse the liposomes.[11-13] Typically, one floating liposome was trapped by optical force and immobilized on the amine-coated surface. Fluorescence images of TOTO-3-labeled enzyme

molecule inside the liposome were then collected by shining the He-Ne laser onto the vesicle. If one was found inside, this liposome (ALP-liposome) was electrofused with another liposome (FDP-liposome) to initiate the enzymatic reaction. Otherwise, a different liposome was trapped. Electrical pulses from a pulse generator (Digitimer Stimulator, DS2A, UK) ranging from 10-30 V with duration 2-10 μs were sufficient to achieve electrofusion.

A mini reaction chamber for electrofusion and incubation was created by placing a silicone spacer onto the amine-coated coverslip. After liposome fusion, the carbon fiber microelectrodes were removed and another regular coverslip (No. 2 Cover Glass, Corning, Corning, NY) was placed on top of the spacer. The chamber allowed long incubation times (hours) and elevated reaction temperatures without drying the droplet. After incubation, the liposome was exposed to the 488 nm laser and the fluorescence signal from the product was registered by the intensified-CCD camera.

Results and Discussion

Single Enzyme Imaging and Manipulation in Liposomes. Single enzyme activities have been studied in capillaries and microfabricated vials.[3-6] In those experiments, highly diluted enzyme solutions were used such that only one enzyme molecule was present in every microvial or discrete zone of the capillary. However, proof of the existence of a single enzyme in the reaction zone was based only on statistical analysis and dilution factors. In this work, single molecules were labeled by fluorescent dyes and the catalytic reactions were carried out in solution confined by the lipid membranes of liposomes, which mimic the biochemical reactions in living systems and avoids interference from the glass wall of the container.

In order to verify that only one ALP molecule was encapsulated in the liposome, we took

images of the liposome-enclosed single protein before electrofusion. Because all liposomes were dialyzed extensively, untrapped enzyme molecules outside the liposomes should be completely absent. However, there were still a few cell traumas due to solution transfer that resulted in the release of enzymes from the liposomes. Fortunately, the very short working distance of the 100× oil-immersion objective helped us to distinguish molecules that were in focus from those that were out of focus. This criterion prevented us from choosing those out-of-focus molecules of free-flowing enzymes. However, leakage of ALP from the liposomes resulted in high background when they react externally and degraded not only image collection but also detection limits. Therefore, we introduced 0.4 μL phosphatase inhibitor to the liposome mixture (20 μL of ALP-liposome and 20 μL FDP-liposome solutions) to suppress reaction (and thus fluorescence) outside the liposomes.

The procedure in each experiment was as follows: (1) collect the bright field image of an immobilized liposome; (2) shine the He-Ne laser and record the fluorescence image of the labeled protein in this liposome; (3) make sure from the image that only one enzyme is present in the liposome, if not, repeat steps (1) and (2); (4) electrofuse the single-ALP-liposome with another liposome; (5) incubate the fused liposome for some period of time; (6) shine the 488-nm laser and record the fluorescence image of the fluorescein-filled liposome.

Figure 2 presents the images of a liposome at different stages. Fig. 2A shows the bright-field image of the single-ALP-liposome. The light source in Fig. 2A was cut off by a 550-nm highpass filter which helped to prevent photobleaching of the TOTO-3 molecules. The bright spot in Fig. 2B represents the fluorescence image of the TOTO-3-labeled single ALP enclosed by the liposome. A comparison between a liposome containing one versus two enzyme molecules is shown in the Supporting Information (Fig. S1). Fig. 2C shows the bright-field image of both

the single-ALP-liposome and FDP-liposome before electrofusion. After initiation of reaction by electrofusion, the high-pass filter was replaced by a 670-nm low-pass filter to prevent photobleaching of the products. The electrofused liposome is shown in Fig. 2D. Note that the diameter is roughly $\sqrt[3]{2}$ of that in Fig. 2A because the volume was doubled. The fusion event triggered mixing of the liposome contents and hence the enzymatic reaction proceeded inside the liposome. The degree of mixing of the contents can be evaluated by considering the diffusion of reactants. It is well known that the mean-square-displacement of molecular diffusion is given by $\langle x^2 \rangle = Dt$, where x is the displacement of the molecule, D is the diffusion coefficient, and t is time. If the elapsed time after electrofusion is 1 s and the diffusion coefficients of FDP and ALP are (estimated) 4.25×10^{-10} and 6.1×10^{-11} m^2/s,[14, 20] the average displacements of FDP and ALP are 21 and 7.8 μm. In our experiments, the size of the liposomes ranged from 3.3 to 11 μm; therefore, the contents were well mixed after several seconds. Compared to the incubation time, the time for thorough mixing was negligible. After incubation for 30 min, the products, fluorescein molecules, were probed by the 488-nm argon ion laser and the fluorescence image of the fused liposome (Fig. 2E) was collected.

Single Enzyme Reactivity in Liposome Reactors. It was reported that up to 99.5% of the proteins could be lost due to adsorption to the wall of the glass pipet in electroinjection.[14] In that case, direct measurement of enzyme concentrations will be problematic and true single-molecule studies will be difficult. Unlike electroinjection of liposomes, adsorption of proteins to glass surfaces will not be an issue in electrofusion. In our experiments, the labeled proteins and the substrates were surrounded only by lipid membranes. Furthermore, from the fluorescence images, it is clear that the protein was moving freely inside the liposome and rarely came in contact with the lipid membrane. After electrofusion of the lipid membranes, the re-

sultant liposome was incubated for a known period of time. The intensity of fluorescence from the fluorescein molecules can be converted into the concentration of products and therefore the activity of the single enzyme molecule in the liposome through a calibration curve (Fig. S2 in Supporting Information). The fluorescence intensities in the calibration curve were obtained by imaging individual liposomes that contain different (known) concentrations of fluorescein. Note that not all fused liposomes produced fluorescent products after incubation. This is because one cannot distinguish between a liposome that contains FDP and one that contains no FDP. The latter is present in the pool of ALP liposomes as zero-molecule entities, as required by Poisson statistics.

The catalytic reaction of transforming FDP into fluorescein by ALP involves more than one step. First FDP is digested by the enzyme and becomes fluorescein monophosphate (FMP), releasing an inorganic phosphate ion (P*i*). FMP can be further digested by the enzyme to produce a strongly fluorescent product, fluorescein, plus another P*i*. In addition, there are two other isomers that may be in equilibrium with FMP.[21] If we considered all rate and equilibrium constants without omission, the rate law of this enzymatic reaction would be quite complicated. Fortunately, the reaction can be treated as a pseudo-first order reaction when the reaction time is long.[14] In this work, the incubation time was in the order of tens of minutes, which was many orders greater than the characteristic time scale.[14] As a consequence, this catalytic reaction can be simplified as an one-step reaction: FDP $\xrightarrow[ALP]{}$ F + 2 P*i*. Further, enzymatic reactions can be treated as pseudo-zeroth order reaction such that the reaction rate is independent of substrate concentrations when the substrate concentrations are large. In this work, the enzyme concentration in the liposomes was in pM level (single molecule) and the substrate concentration in the liposomes was 10 μM, which was 5-6 orders higher than the concentration of enzyme molecules.

As a result, it is reasonable to assume that single ALP molecules reach their maximum reaction velocity, V_{max}, during the incubation time and the reaction can be treated as a zeroth-order reaction.

Fig. 3 presents the results of single-molecule reactions. For 30 single ALP molecules, the mean activity is 272 s^{-1} with a standard deviation of 206 s^{-1}. The broad distribution appears to show two maxima centered at 150 and 450 s^{-1} along with a few high activity molecules. In bulk experiments, we measured the activity to be 168 s^{-1} (Fig. S3 in Supporting Information). The lower value for bulk experiments may reflect loss of enzyme in transferring reagents. Also, the difference in activities between the labeled and unlabeled enzymes was found to be only 4% (Fig. S4 in Supporting Information). Previously, for different buffer systems, single molecule studies gave 108 s^{-1} [5] and bulk studies gave 380 s^{-1} [5] and 400 s^{-1}.[14]

Several different sources may account for the broad and non-Gaussian distribution. Glycosylation of proteins may contribute to heterogeneity.[5,22] Glycosylation affects both the flexibility and the dynamic stability of proteins and has been shown to cause a 4-fold variation in reactivity.[22] However, a variation of ~ 20-fold in protein activity (this work and Ref. 3) cannot be attributed solely to different glycoforms. Recent results from reaction-induced infrared spectroscopy showed that the binding of P*i* to the active site of bovine intestinal ALPs led to a distortion of the polypeptide carbonyl backbone of the enzyme.[23] These results also explained the well-known fact that the phosphate molecules are inhibitors of ALPs. Therefore, we can conclude that the phosphate-induced structural change is another major reason for the broad and non-Gaussian distribution of the activities of bovine intestinal ALP molecules.

Conclusions

Single-molecule reactions are carried out in liposome reactors. The use of fluorescent marker along with an appropriate substrate allowed us to monitor true single-molecule reactivity in a cell-like environment. The activities of individual alkaline phosphatase molecules from bovine intestinal mucosa showed a wide distribution. Both phosphate-induced structural change at the active site and glycosylation are likely to be responsible for this highly heterogeneous behavior.

This demonstration has many potential applications. The use of the biomimetic containers allows us to detect single-molecule activity at different intracellular and extracellular conditions. For example, one can incorporate liposomes containers with transmembrane molecular/ion channels and create a concentration gradient which is very similar to cell environments to study how biomolecules response to external changes. In such a system, the kinetics and dynamics of biomolecular reactions can be studied at the ultimate low concentration, i.e., single-molecule level, without undesirable interferences from other biological cofactors or artificial containers.

References

1. Hiromi, K. *Kinetics of Fast Enzyme Reactions*; Kodansha Ltd.: Japan, 1979.
2. Yeung, E. S. *Annu. Rev. Phys. Chem.* **2004**, *55*, 97-126.
3. Xue, Q.; Yeung, E. S. *Nature* **1995**, *373*, 681-683.
4. Tan, W.; Yeung, E. S. *Anal. Chem.* **1997**, *69*, 4242-4248.
5. Craig, D. B.; Arriaga, E. A.; Wong, J. C. Y.; Lu, H.; Dovichi, N. J. *J. Am. Chem. Soc.*

1996, *118*, 5245-5253.

6. Lu, H. P.; Xun, L.; Xie, X. S. *Science* **1998**, *282*, 1877-1882.
7. Li, H.-W.; Yeung, E. S. *Anal. Chem.* **2005**, *77*, 4374-4377.
8. Xu, X.; Yeung, E. S. *Science* **1997**, *275*, 1106-1109.
9. Xu, X.-H.; Yeung, E. S. *Science* **1998**, *281*, 1650-1653.
10. Polakowski, R.; Craig, D. B.; Skelley, A.; Dovichi, N. J. *J. Am. Chem. Soc.* **2000**, *122*, 4853-4855.
11. Chiu, D. T.; Wilson, C.; Ryttsen, F.; Stromberg, A.; Farre, C.; Karlsson, A.; Nordholm, S.; Gaggar, A.; Modi, B. P.; Moscho, A.; Garza-Lopez, R. A.; Orwar, O.; Zare, R. N. *Science* **1999**, *283*, 1892-1895.
12. Chiu, D. T.; Wilson, C. F.; Karlsson, A.; Danielsson, A.; Lundqvist, A.; Stromberg, A.; Ryttsen, F.; Davidson, M.; Nordholm, S.; Orwar, O.; Zare, R. N. *Chem. Phys.* **1999**, *247*, 133-139.
13. Strömberg, A.; Karlsson, A.; Ryttsén, F.; Davidson, M.; Chiu, D. T.; Orwar, O. *Anal. Chem.* **2001**, *73*, 126-130.
14. Karlsson, A.; Scott, K.; Markström, M.; Davidson, M.; Konkoli, Z.; Orwar, O. *J. Phys. Chem. B* **2005**, *109*, 1609-1617.
15. Sott, K.; Lobovkina, T.; Lizana, L.; Tokarz, M.; Bauer, B.; Konkoli, Z.; Orwar, O. *Nano Lett.* **2006**, *6*, 209-214.
16. Kulin, S. K.; Kishore, R.; Helmerson, K.; Locascio, L. *Langmuir* **2003**, *19*, 8206-8210.
17. Jesorka, A.; Markstrom, M.; Orwar, O. *Langmuir* **2005**, *21*, 1230-1237.
18. Moscho, A.; Orwar, O.; Chiu, D. T.; Modi, B. P.; Zare, R. N. *PNAS* **1996**, *93*, 11443-11447.

19. Ashkin, A.; Dziedzic, J. M.; Bjorkholm, J. E.; Chu, S. *Optics Lett.* **1986**, *11*, 288.

20. Leach, A. M.; Wheeler, A. R.; Zare, R. N. *Anal. Chem.* **2003**, *75*, 967-972.

21. Huang, Z.; Wang, Q.; Ly, H. D.; Gorvindarajan, A.; Scheigetz, J.; Zamboni, R.; Desmarais, S.; Ramachandran, C. *J. Biomol. Screen.* **1999**, *4*, 327-334.

22. Rudd, P. M.; Joao, H. C.; Coghill, E.; Fiten, P.; Saunders, M. R.; Opdenakker, G.; Dwek, R. A. *Biochem.* **1994**, *33*, 17-22.

23. Zhang, L.; Buchet, R.; Azzar, G. *Biophys. J.* **2004**, *86*, 3873-3881.

Figure Captions

Figure 1. Experimental setup for single-molecule reactions in liposome reactors. The pink beam (808 nm) from near-IR laser is collimated by a pair of lenses and is used to trap vesicles onto the amine-coated coverslip. The 632.8 nm HeNe laser is used to excite TOTO-3-labeled proteins. The 488 nm argon ion laser is used to probe the products of the enzymatic reactions. Two 3-D translation stages are used to position carbon fiber microelectrodes for electrofusion of liposomes. Fluorescence signals are collected by an intensified CCD camera and processed by a desktop computer. M: mirror; BC: beam collimator; DC1 and DC2: dichroic mirrors, PC: polychroic mirror; BP: bandpass filter; DC: direct current power supply for short electrical pulses.

Figure 2. Images of liposomes at different stages. (A) Bright-field image of the ALP-liposome. (B) Fluorescence images of one TOTO-3-labeled ALP in the liposome. (C) Bright-field image of the liposomes prior to electrofusion. (D) Bright-field image of the fused liposome. (E) Fluorescence image of the fused liposome after incubation. Bar = 5 μm.

Figure 3. Histogram of activities of 30 single alkaline phosphatase molecules from bovine intestinal mucosa. Reaction rates were calculated from reaction times and fluorescein concentrations that were obtained by converting the integrated fluorescence signal using Fig. S2 in Supporting Information.

Figure S1. Fluorescence images of liposomes containing ALP. Left, one molecule; and right, two molecules.

Figure S2. Calibration curve for fluorescein concentrations in liposomes.

Figure S3. Bulk experiment of ALP and FDP. Reaction condition: FDP = 3.3 μM, ALP = 161 pM. In 70 s, 1890 nM fluorescein was produced.

Figure S4. Comparison of the activities of dye-labeled ALP vs. regular ALP. Experimental conditions: FDP = 6.6 μM, ALP = 10.9 pM. Yellow triangular dots: labeled enzyme. Pink rectangular dots: regular enzyme. The slope indicates the relative activity: 9.7971/9.4304 = 1.039.

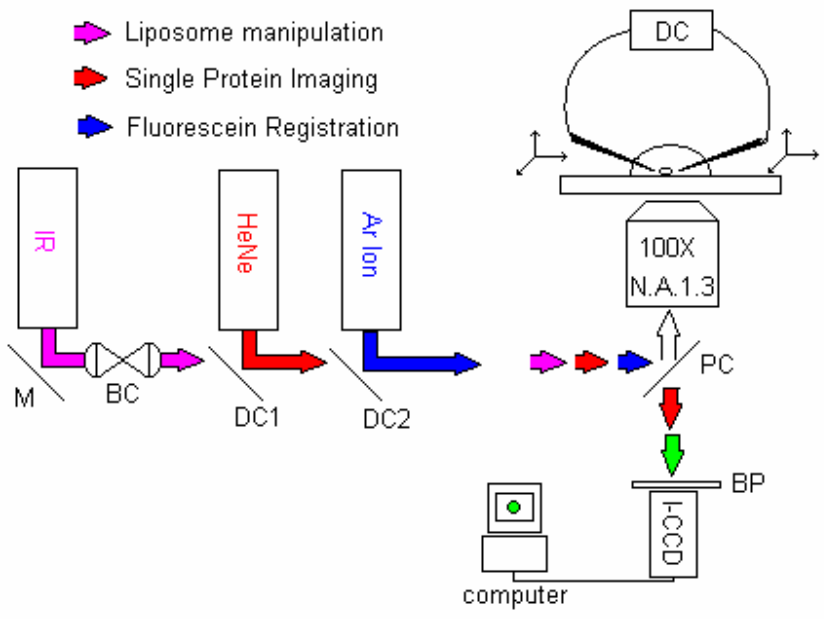

Figure 1.

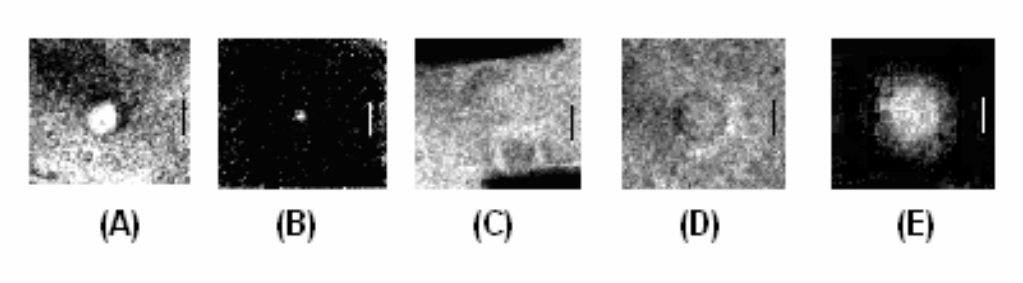

Figure 2.

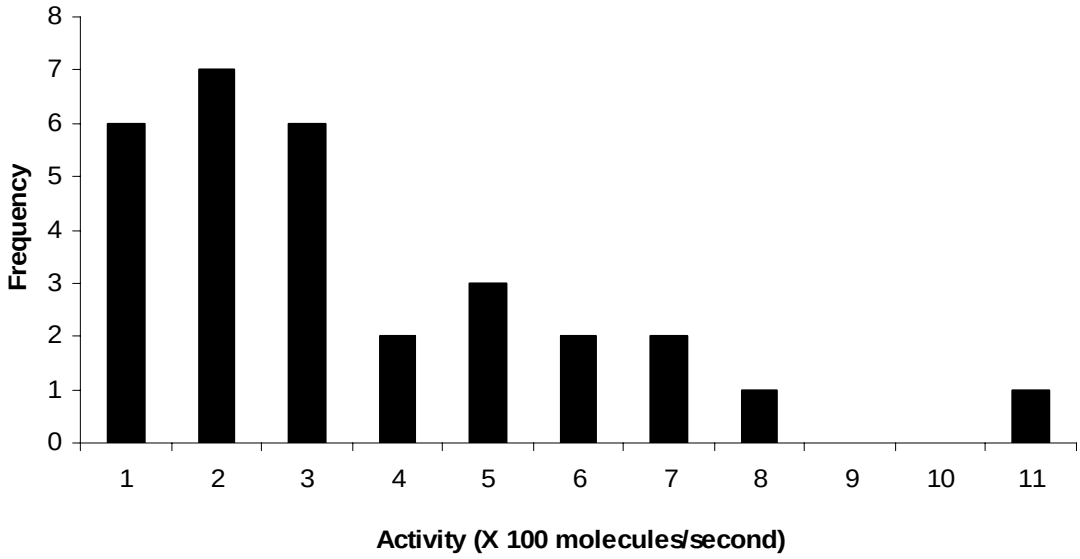

Figure 3.

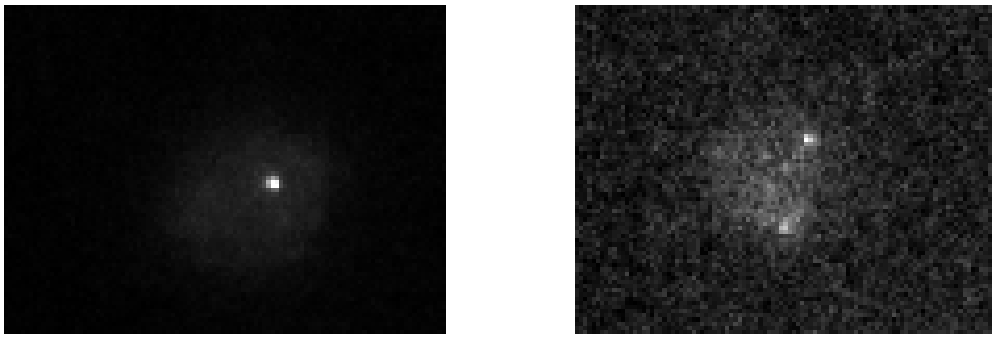

Figure S1.

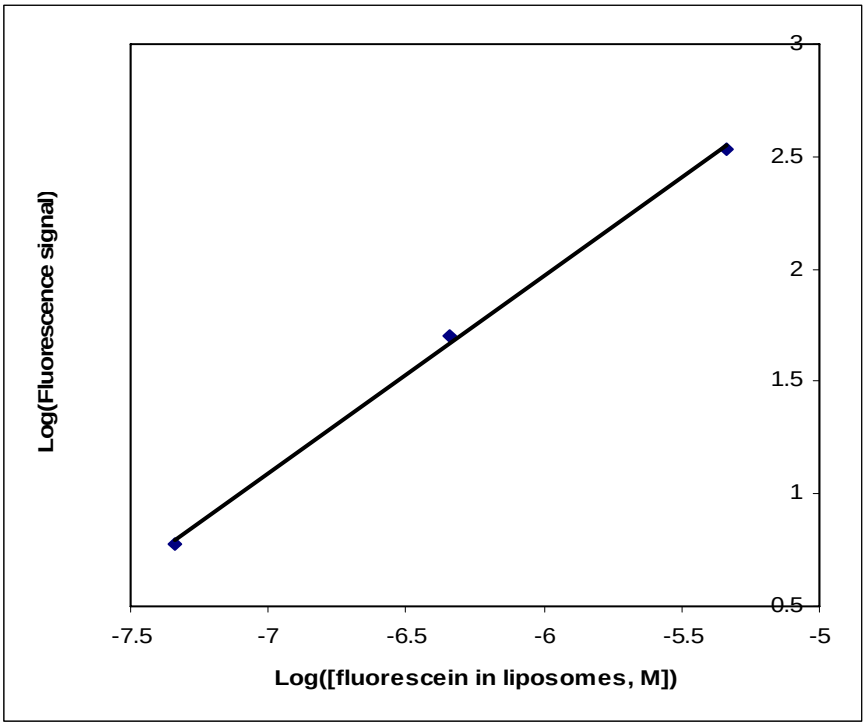

Figure S2.

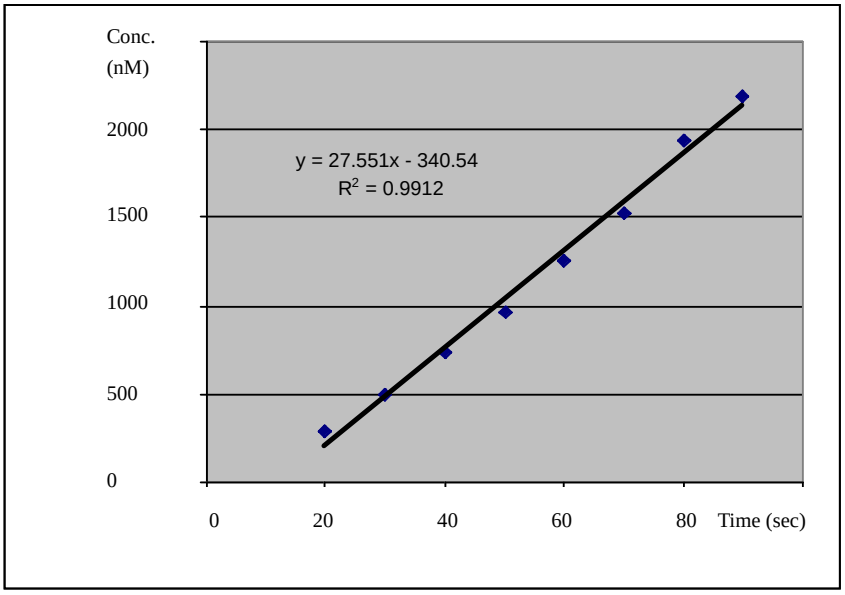

Figure S3.

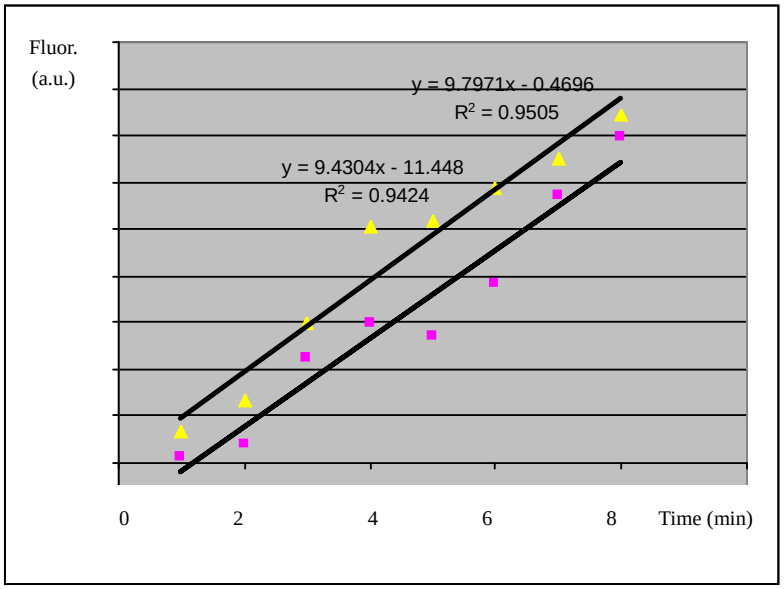

Figure S4.

CHAPTER 6. GENERAL CONCLUSIONS

A thorough understanding of molecular properties of different aspects demands various probing techniques. In this thesis, we utilized several optical detection and spectroscopic techniques to study not only physical but also chemical behaviors of molecules. Important physical characteristics of molecules such as excitation energy transfer rate and structural heterogeneity of guest-host systems were obtained by using low-temperature frequency-domain laser spectroscopy; time-domain laser spectroscopy offered the dynamic information of molecular vibrations of very short time scale. Also, the marriage of liposome techniques and laser-induced fluorescence provided accurate measurements of molecular reactions and revealed heterogeneous nature of individual enzyme activity. In the near future, we can foresee that the combinations of these probing techniques will provide new insight and comprehensive information to many important biochemical and biophysical problems, such as metabolisms of single protein in living cells.

ACKNOWLEDGEMENT

For my five years' graduate life, there are two professors who are the most important: Dr. Small and Dr. Yeung. Dr. Small, my first advisor, recruited me from Taiwan and gave me the opportunity to pursue higher education; Dr. Yeung, my last advisor, supported me in every aspect, especially in finishing my Ph.D. program. Their precious advice and helping hands along the way will be remembered and deeply appreciated. I am also thankful to my second advisor, Dr. Stauffer, who showed me the world of femtochemistry and taught me the techniques of laser alignment. In addition, I would like to mention my gratitude to Dr. Lin, Dr. Schmidt-Rohr, and Dr. Song, who serve on my POS committee and gave me important advice when I was in need of them.

Much of my background of physical chemistry was built in the years of the Small group. All the scientists, Drs. Reinot, Zazubovich, Hayes, and Jankowiak, in the Small group were being great teachers and friends. I am thankful for their teaching and lecturing from low temperature physics, laser spectroscopy, to many other advanced subjects in science. Among them, I appreciate Tonu Reinot the most: for his providing important suggestions to every project of mine. To Kerry Riley and Nhan Dang, I thank you for being supportive and good friends in all the years and revising my thesis (Kerry).

Lastly, I would like to dedicate this dissertation to my family, especially to Grandpa, Dad and Mom, who raised me, educated me, and are always being there for me. Without your total support, I would not be able to come all the way from Taiwan to the U.S.A. I have to express my gratitude to my wife, Cherry, for taking good care of me and "Little Bobby", and for her company for all these years.